# Supporting Information

## Photochemical-Co-Mechanical Polishing for Silicon Wafer Using a Janus $CeO_2$ Slurry

Yuhang Qi[1*], Jinghui Lai[1], Zihan Luo[2], Shengying Yue[2*], Yuan Li[3], Shiguang Guo[1], Ziyang Li[1], Guofeng Pan[1], Xueli Yang[1], Chong Luo[1], Shuxin Ouyang[3*]

[1]Tianjin Key Laboratory of Electronic Materials and Devices, School of Electronics and Information Engineering, Hebei University of Technology, Tianjin 300401, China

[2]State Key Laboratory for Strength and Vibration of Mechanical Structures, School of Aerospace, Xi'an Jiaotong University, Xi'an 710049, China

[3]Engineering Research Center of Photoenergy Utilization for Pollution Control and Carbon Reduction, College of Chemistry, Central China Normal University, Wuhan, 430079 China

# Supplementary Methods

## Materials

All solutions used in this study were prepared with deionized water, and the abrasive was cerium oxide (99.95% purity, supplied by Shanghai Aladdin Biochemical Technology Co., Ltd.). All chemical reagents were of analytical grade. Unless otherwise specified, all solutions in this paper have a pH of 10. Chemical agents utilized encompass: hydrogen peroxide ($H_2O_2$; with a purity of 30%, supplied by Tianjin Fengchuan Chemical Reagent Technology Co., Ltd.), PVP 99% pure, supplied by Shanghai Aladdin Biochemical Technology Co., Ltd.), silica sol (40% purity, supplied by Jinwei Group Co., Ltd.). Titanium Oxide ($TiO_2$; 99.9% pure, supplied by Shanghai Aladdin Biochemical Technology Co., Ltd.), aluminium oxide ($Al_2O_3$; 99% pure, supplied by Shanghai Dibo Chemicals Technology Co., Ltd.), ferric oxide ($Fe_2O_3$; 99.5% pure, supplied by Shanghai Dibo Chemicals Technology Co., Ltd.), zinc oxide (ZnO; 99.9% pure, supplied by Meryer (Shanghai) Biochemical Technology Co., Ltd.), strontium titanate ($SrTiO_3$; 99% pure, supplied by Bide Pharmatech Co., Ltd.), tungsten trioxide ($WO_3$; 99.8% pure, supplied by Anhui Zesheng Technology Co., Ltd.), stannic oxide ($SnO_2$; 99.5% pure, supplied by Shanghai Macklin Biochemical Technology Co., Ltd.), cadmium oxide (CdO; 99.99% pure, supplied by Beijing innoChem Science & Technology Co., Ltd.), zirconium dioxide ($ZrO_2$; 99.99% pure, supplied by Mreda Technology Co., Ltd.), benzoquinone (BQ, $C_6H_4O_2$; 99% pure, supplied by Mreda Technology Co., Ltd.), methanol (MeOH, $CH_4O$; 99% pure, supplied by Shanghai Macklin Biochemical Technology Co., Ltd.), perfluorosulfonic acid-PTFE copolymer (nafion; 5% pure, supplied by E.I.Du Pont Company), potassium hydroxide

(KOH; 99.9% pure, supplied by Shanghai Aladdin Biochemical Technology Co., Ltd.).

**Electrochemical Experiment**

All electrochemical tests were performed using the CHI660E electrochemical workstation from Shanghai Chenhua Instruments Co., Ltd.

he corrosion properties of Si in designated solutions were investigated. Data for open circuit potential (OCP), dynamic potential polarization (Tafel plots), and impedance spectrum (EIS) were collected using a three-electrode system, with Si as the working electrode, standard calomel electrode (SCE) as the reference, and platinum as the counter electrode. Before each test, the Si electrode was sealed using insulating tape, revealing a 1 $cm^2$ active area. Before each electrochemical measurement, the samples were immersed in 5 wt% potassium hydroxide solution for 5 min to remove the natural oxide layer. This was followed by rinsing with deionized water and drying with compressed air. The OCP was stabilized for around 600 seconds to ensure the acquisition of trustworthy and consistent potential readings. Potentiodynamic polarization was measured within a voltage range of OCP ± 0.3 V at a scan rate of 5 mV/s. EIS was performed at the OCP, spanning a frequency range of 0.01 Hz to 1000 kHz, with a 5 mV AC signal applied. EIS data were analyzed and modeled using Zview software.

A uniform ink was prepared by dispersing 10 mg of the catalyst into 420 μL of a solution containing 200 μL of isopropanol, 200 μL of deionized water, and 20 μL of Nafion solution, followed by 30 minutes of ultrasonication. The resulting ink was evenly applied onto FTO glass,

with insulating tape to ensure exposure of a 1 $cm^2$ active area. Next, the prepared electrode was annealed at 200°C for 2 hours.

The transient photocurrent response measurements were conducted using a standard three-electrode system. Pt and Ag/AgCl electrodes served as the counter and reference electrodes, respectively, and the as-prepared electrode was used as the working electrode. Among these measurements, the applied potential was 1 V vs. Ag/AgCl. The EIS measurements were performed at the open circuit potential, ranging from 0.01 Hz to 1000 kHz. For these experiments, 0.5 mol/L KOH solution was used as the electrolyte, and a 300 W Xe lamp served as the light source.

The ORR measurements were conducted using a standard three-electrode system, with Pt and Ag/AgCl electrodes serving as the counter and reference electrodes, respectively, and the as-prepared disk-ring electrode (5.61 mm in diameter, with an electrode surface area of 0.2475 $cm^2$) being used as the working electrode (Pine Research Instrumentation). Linear sweep voltammetry (LSV) measurements were recorded in an $O_2$-saturated 0.5 M KOH electrolyte solution with a scan rate of 5 mV/s and a rotating speed of 1600 rpm. The potentials vs. Ag/AgCl were converted to the RHE scale by the following equation:

$$E_{RHE} = E_{Ag/AgCl} + 0.098 + 0.059 \times \mathrm{pH}$$

In calculating the bandgap and DOS, the Geometry Optimization adopt the DFT + U approach to improve the description of strong on-site Coulomb repulsion of Ce 4 f electrons. U-J was set to 6.0 eV, which has been widely reported to be effective. The cutoff energy of 400 eV was used for all calculations, the k-point mesh of 4×4×4 was used, the energy tolerance accuracy was set to $1\times10^{-5}$ eV/atom, and the k-point was set to 8×8×8. The maximum force was selected at 0.03 eV/Å, and the

maximum atom displacement was placed at $1\times10^{-3}$ Å. The calculations of band structure and density of states were performed using a cutoff energy of 450 eV. For the Brillouin-zone sampling, we used the 4 × 4 × 4 Monkhorst-Pack mesh, and the self-consistent convergence of the total energy is $2.0\times10^{-6}$ eV/atom. The d-band center calculation is shown in the following equation:

$$\varepsilon_d = \frac{\int_{-\infty}^{\infty} n_d(\varepsilon)\varepsilon d\varepsilon}{\int_{-\infty}^{\infty} n_d(\varepsilon) d\varepsilon}$$

In calculating the electron density difference and surface $O_V$ formation energy, the Geometry Optimization of the experimental effect of the GGA + U method with U = 5 eV for the reduction of $CeO_2$ under UV irradiation for the Ce 4f state. A model of 16.199 Å was cleaved using $CeO_2$ (111) as a section, from which supercells were built in the range of 2 × 2 × 1, and then a vacuum layer of 15 Å thickness was created. The cutoff energy of 400 eV was used for all calculations, the k-point mesh of 1×1×1 was used, the energy tolerance accuracy was set to $1\times10^{-5}$ eV/atom, and the k-point was set to 2×2×2. The maximum force was selected at 0.02 eV/Å, and the maximum atom displacement was placed at $1\times10^{-3}$ Å. The calculations of electron density difference were performed using a cutoff energy of 400 eV, for the Brillouin-zone sampling, we used the 4 × 4 × 4 Monkhorst–Pack mesh, and the self-consistent convergence of the total energy is $2.0\times10^{-6}$ eV/atom. The $O_V$ formation energy calculation is shown in the following equation:

$$E_v^f = \frac{E_{CeO_{2-x}} - E_{CeO_2}}{x} + \frac{1}{2}E_{O_2}$$

## Characterization

Raman spectra were recorded using the Horiba (Xplora Plus) instrument. The contact angle is measured by a contact angle measuring instrument (Powereach, JC2000D). The element concentration was measured using a Thermo Scientific ICP-MS. Friction and temperature were measured using GnP POLI-500 (G&P Technology, Inc). The specific surface areas and pore size distribution were evaluated by the BET method using N2 adsorption (Micromeritics, ASAP 2460). Hydrogen temperature-programmed reduction ($H_2$-TPR) and oxygen temperature-programmed desorption ($O_2$-TPD) measurements were performed using a BELCAT II system (MicrotracBEL, Japan). Thermal imaging is captured by Infrared thermal imager (Fluke, Fluke-Ti300). For $H_2$-TPR, the sample was pretreated under an argon flow (30 mL/min) by heating from room temperature to 300 °C at a rate of 10 °C/min and holding for 60 min. After cooling to 50 °C, a 10% $H_2$/Ar gas mixture (50 mL/min) was introduced for 0.5 h. Once the baseline stabilized, the temperature was increased to 800 °C at a rate of 10 °C/min under a 10% $H_2$/Ar flow (30 mL/min). For $O_2$-TPD, the sample was similarly pretreated in helium at 300 °C for 1 h. After cooling and stabilization, a 10% $O_2$/Ar gas mixture (50 mL/min) was introduced for 0.5 h. The sample was then heated to 800 °C at 10 °C/min under a 10% $O_2$/Ar flow (30 mL/min). Current–voltage (I–V) characteristics were measured using an Agilent B1500A Semiconductor Device Analyzer in conjunction with an EverBeing EB-8 probe station.

The X-ray Photoelectron Spectroscopy (XPS) instrument utilized in this research was the ESCALAB250Xi model, manufactured by Thermo Scientific. After testing, the XPS spectra were analyzed using CasaXPS software and calibrated based on the

C1s peak (284.6 eV). The amount of $Ce^{3+}$ was calculated based on the Ce 3d XPS spectra as the following equation:

$$p\ (Ce^{3+}) = \frac{Ce^{3+}}{Ce^{4+} + Ce^{3+}} \times 100\%$$

The density of $O_V$ was calculated based on the O 1S XPS spectra as the following equation:

$$p\ (O_V) = \frac{O_V}{O_V + O_L + O_C} \times 100\%$$

The diffuse reflection spectra were measured by UV–Vis spectrophotometer (PerkinElmer, Lambda 1050+). The bandgap energy ($E_g$) was calculated as the following formula:

$$\alpha h\nu = A(h\nu - Eg)^n$$

where A, h, ν, and α are constant values that refer to a constant, Plank constant, light frequency and absorption coefficient, respectively.

## Calculation details

The PWmat program with GPU acceleration was employed to investigate the peak-to-valley difference of the Si (100) surface based on density functional theory (DFT). The exchange-correlation interactions were treated using the Perdew-Burke-Ernzerhof (PBE) functional within the generalized gradient approximation (GGA). Norm-conserving pseudopotentials were utilized, and the plane-wave energy cutoff was set to 544 eV. The surface model consisted of three atomic layers and a vacuum region of 15 Å. Structural optimization was performed with convergence criteria of forces less than 0.1 eV $Å^{-1}$ and energy changes below $10^{-4}$ eV. Converged energy: $E = -1.362572371481 \times 10^4$ eV.

# Supplementary Figures

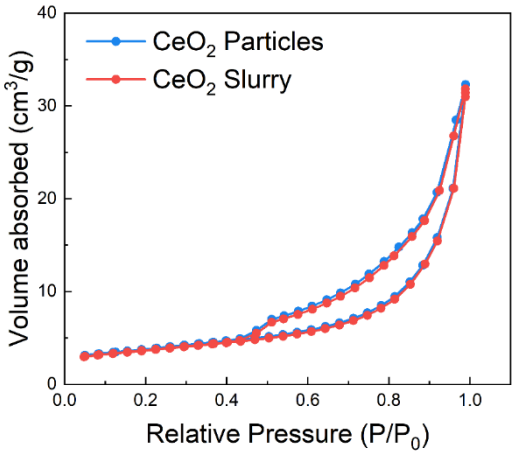


**Supplementary Fig. S1.** BET surface area of $CeO_2$ particles and $CeO_2$ slurry.

**Discussion:** The specific surface areas of $CeO_2$ particles and $CeO_2$ slurry were measured using the Brunauer–Emmett–Teller (BET). The specific surface area of $CeO_2$ particles was 13.26 $m^2/g$, whereas that of the $CeO_2$ slurry was slightly lower, at 12.92 $m^2/g$. This minor reduction indicates that the slurry preparation process has a negligible impact on the overall surface area of the $CeO_2$ material. Additionally, the nitrogen adsorption-desorption isotherms for both samples exhibited a typical type IV profile with a prominent hysteresis loop characteristic of mesoporous structures.

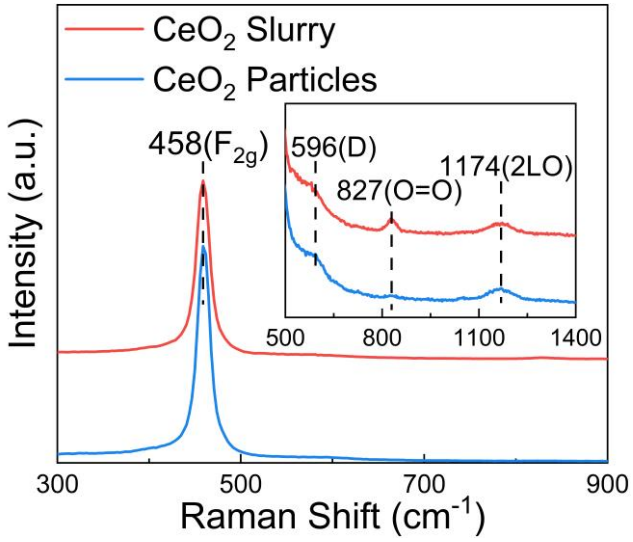


**Supplementary Fig. S2.** Raman spectrum, inset: the 500-1300 $cm^{-1}$ shift region.

**Discussion:** The $CeO_2$ particles were primarily characterized by a peak at 458 $cm^{-1}$, corresponding to the $F_{2g}$ mode of the $CeO_2$ lattice[1]. Additional peaks at 596 $cm^{-1}$, 827 $cm^{-1}$, and 1174 $cm^{-1}$ were associated with defect-induced modes (D), adsorbed peroxo/superoxo species (O–O stretching), and longitudinal optical (2LO)[2]. Adsorbed $O_2^{2-}/O_2^-$ species act as intermediates in the re-oxidation of reduced $CeO_{2-x}$ to $CeO_2$[3]. Electrons donated by $Ce^{3+}$ cations drive their conversion to $Ce^{3+}$.

The ratio of the $F_{2g}$ to defect peak intensities ($I_{F2g}$ / $I_D$) serves as a sensitive measure of lattice order versus defectiveness. A higher ratio indicates better crystallinity and fewer defects, while a lower ratio reflects increased lattice disorder from oxygen vacancies, dopant effects, or other imperfections. In Fig. S2, these ratios are 44.16 for $CeO_2$ particles and 38.64 for $CeO_2$ slurry, confirming a higher defect concentration in the slurry.

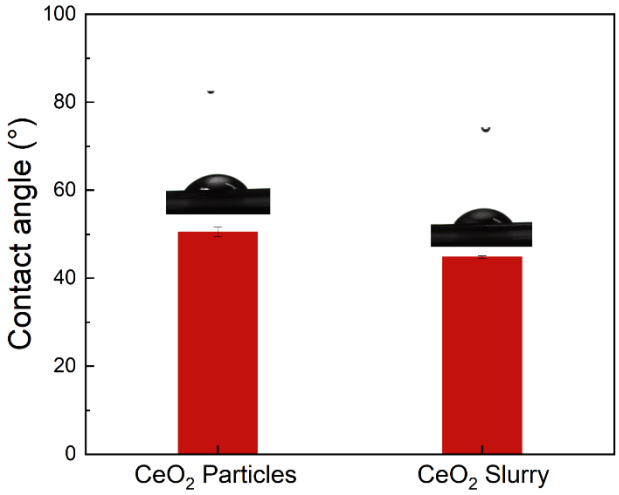


**Supplementary Fig. S3.** Contact angle of $CeO_2$ particles and $CeO_2$ slurry layer on Si wafers surface with deionized water.

**Discussion:** Introducing oxygen vacancies leads to enhanced surface charge accumulation, which reduces particle agglomeration and accounts for the observed decrease in zeta potential. Moreover, oxygen vacancies increase the surface free energy, promoting more effective interactions between the $CeO_2$ abrasive and Si wafers. This effect is supported by contact angle measurements, where the $CeO_2$ slurry demonstrated a reduced contact angle of 44.56°, representing a decrease of 5.93° compared to $CeO_2$ particles. This reduction is attributed to the increased hydrophilicity resulting from water dissociative adsorption on the $CeO_2$ surface following the introduction of oxygen vacancies.

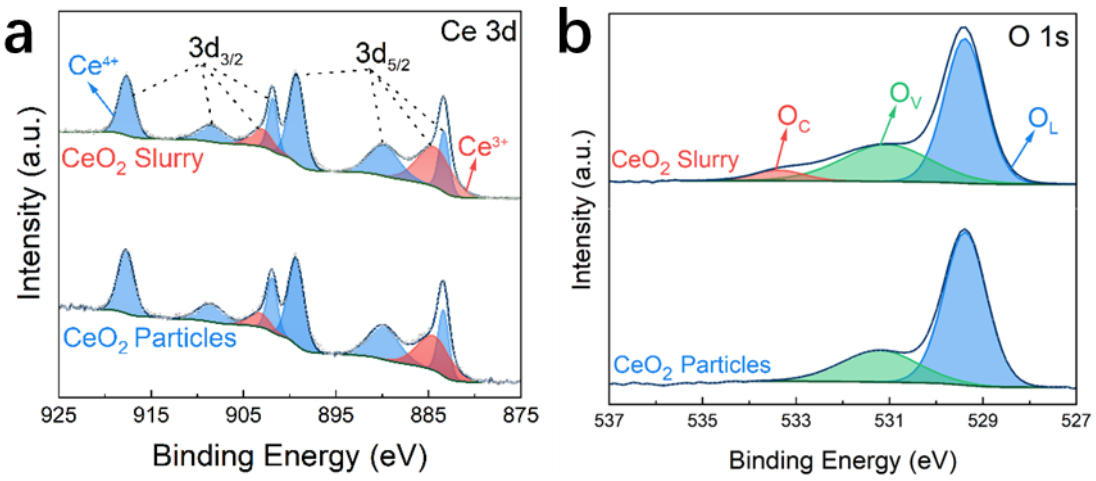


214 **Supplementary Fig. S4. a** Ce 3d, **b** O 1s XPS spectra of $CeO_2$ particles and $CeO_2$
215 slurry.

216

217 **Discussion:** The Ce 3d spectra (Fig. S4a) comprise five spin-orbit split
218 double peaks ($3d_{3/2}$, $3d_{5/2}$), with 903.4 eV and 885.2 eV corresponding to
219 $Ce^{3+}$ signals[4]. Combined with the O 1s spectra (Fig. S4b), the results
220 indicate that Janus $CeO_2$ slurry has a higher concentration of active sites.
221 The relative contents of $Ce^{3+}$ and oxygen vacancies are summarized in
222 Table S1. The O 1s XPS spectrum shows peaks at 531.17 eV and 529.37
223 eV, which are attributed to oxygen vacancies ($O_V$) and lattice oxygen
224 ($O_L$), respectively, while the peak at 533.36 eV corresponds to
225 chemisorbed oxygen species ($O_C$). Calculations indicate that the $O_V$
226 density is 30.17% in $CeO_2$ particles and increases to 34.02% in the $CeO_2$
227 slurry. The $O_C$ originate from adsorbed peroxides ($O_2^{2-}$/$O_2^-$) on the $CeO_2$
228 surface.

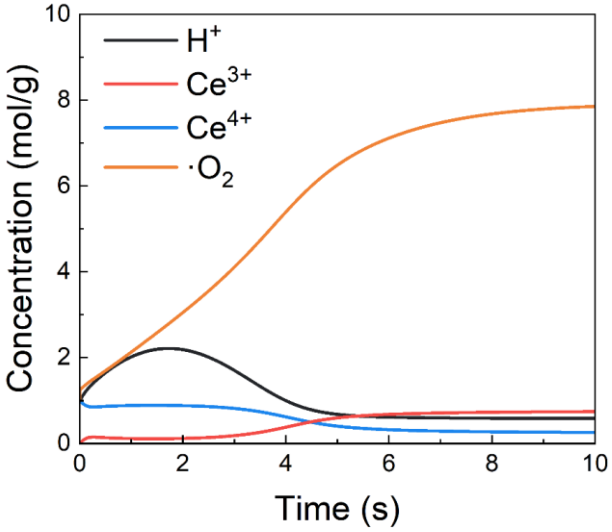


**Supplementary Fig. S5.** Disproportionation reaction of $CeO_2$ with $H_2O_2$ under alkaline conditions.

**Discussion:** During the photocatalytic CMP process, oxygen vacancy concentration of $CeO_2$ increases when $CeO_2$ is combined with $H_2O_2$. Oxygen vacancies migrate to energetically favorable lattice positions, and $Ce^{3+}$ relocates to the crystal surface. Due to the increased ionic radius, they are better accommodated spatially[5]. For this mechanism, a reasonable model for the superoxide disproportionation reaction mechanism at the cerium dioxide nanoparticle surface[6].

The $CeO_2$ slurry shows alkalinity. Therefore, the Runge-Kutta method was used for modeling. Under alkaline conditions, the conversion between $Ce^{3+}$ and $Ce^{4+}$ occurs and eventually reaches equilibrium. When hydrogen peroxide is added, $Ce^{4+}$ actively controls the superoxide, resulting in a minor transformation of $Ce^{3+}$ ions, leading to oxygen vacancies.

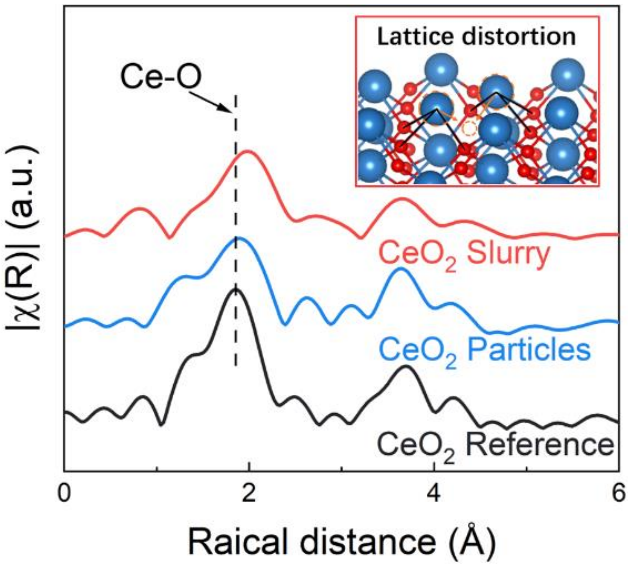


**Supplementary Fig. S6.** Radial distribution function from EXAFS, inset: lattice distortion and coordination environment change in $CeO_2$ slurry.

**Discussion:** The R-space spectra and fitting data (Table S2) further reveal variations in the Ce-O bond length within the $CeO_2$ slurry. Introducing oxygen vacancies results in the elongation of first-shell Ce-O bonds, leading to surface lattice distortion. These findings are further supported by the K-space EXAFS fitting spectra and wavelet transform analysis.

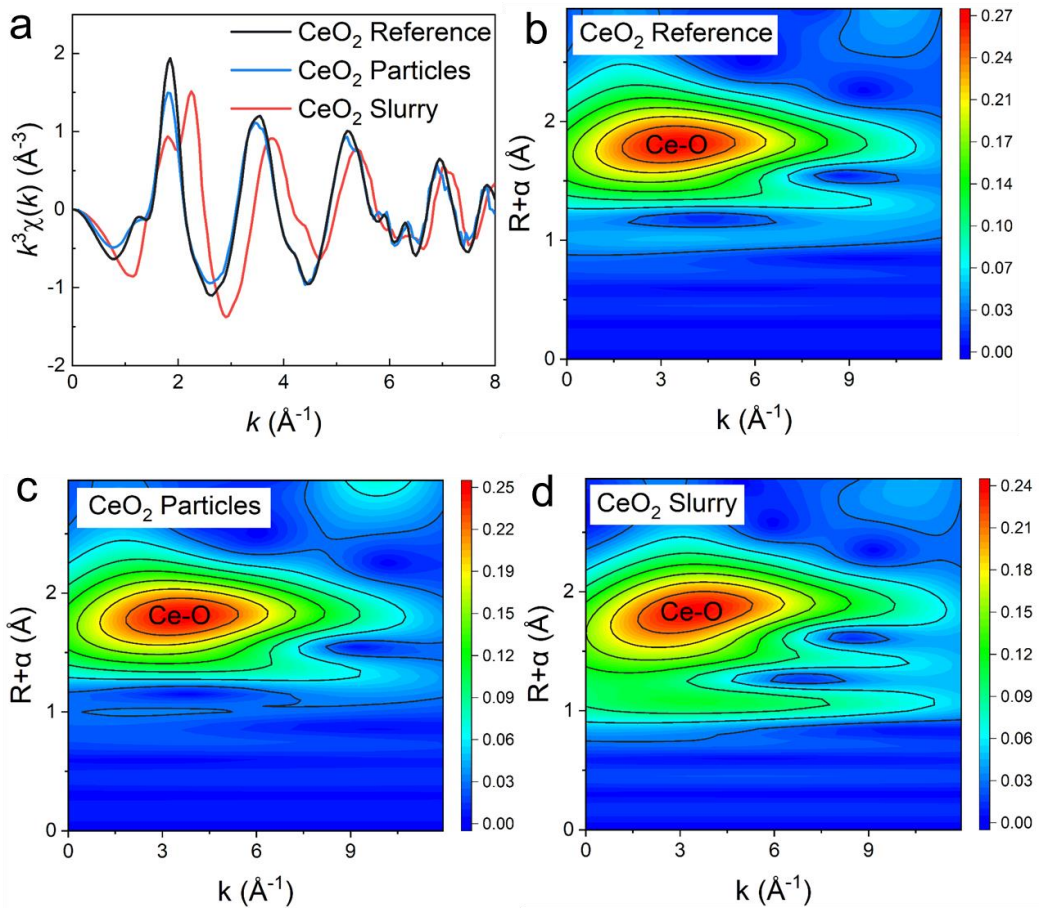


**Supplementary Fig. S7. a** The corresponding K space EXAFS fitting spectra of $CeO_2$ reference, $CeO_2$ particles, and $CeO_2$ slurry. Wavelet transform of Ce K-edge EXAFS spectra for **b** $CeO_2$ reference, **c** $CeO_2$ particles, and **d** $CeO_2$ slurry.

**Discussion:** Combining the results of the EXAFS fits (Table S2) reveals a lower coordination number and a higher Debye-Waller factor for the $CeO_2$ slurry, suggesting a more disordered surface structure. Additionally, oxygen vacancies partially contribute to the Ce-O-Ce shell, thereby promoting greater electron delocalization.

The local chemical environment and physical structure around the Ce atoms were investigated using Ce K-edge EXAFS spectra. From the wavelet transform contour plots (Fig. S7a), each sample exhibited distinct maxima attributed to the scattering effect of neighboring O atoms (Ce-O bonding, first shell, k~3.6 $Å^{-1}$). Compared to the CeO2 reference and

$CeO_2$ particles, the intensity of Ce-O bonding was significantly reduced for the $CeO_2$ slurry, indicating a higher concentration of oxygen vacancies. This reduction is attributed to homogeneous interfaces that disrupt the Ce atom arrays, inducing lattice distortions and suppressing multiple scattering of photoelectrons. Correspondingly, the Ce-O coordination numbers quantitatively support these findings.

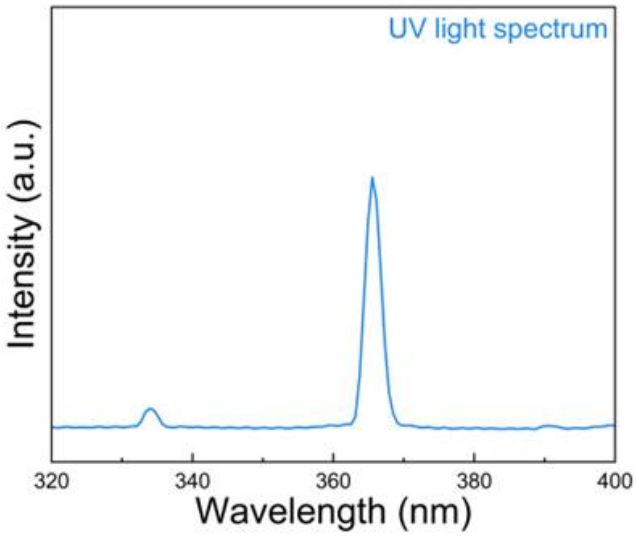


**Supplementary Fig. S8.** Emission spectrum of the UV light source centered at 365 nm.

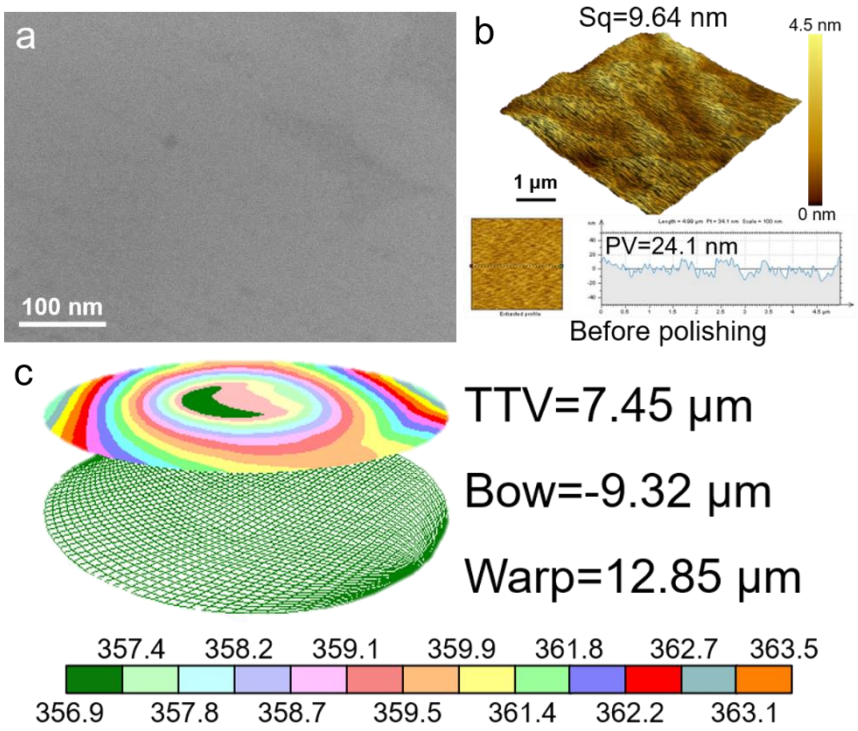


275 **Supplementary Fig. S9. a** 3D AFM image and height profiles. **b** SEM image. **c**
276 Geometric parameter image of Si CMP using $CeO_2$ particles.

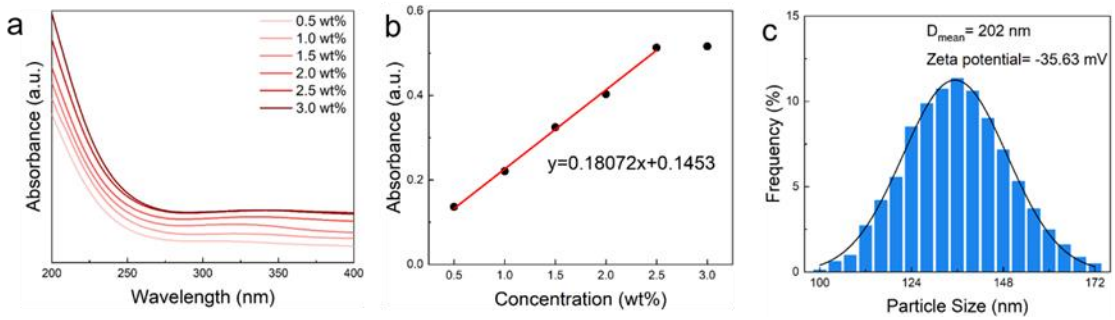


**Supplementary Fig. S10.** (a) UV-Vis absorption spectra of $CeO_2$ slurry of different concentrations. (b) This fit shows a linear trend with a slope of 0.18072 called the exponent coefficient. (c) Particle size distribution histogram and zeta potential of 3 wt.% $CeO_2$, which exhibits an average $CeO_2$ particle size of 136.5 nm and zeta potential of -35.63 mV.

**Discussion:** The intensity of the characteristic absorption peak gradually increased, with the $CeO_2$ slurry reaching maximum absorbance at a concentration of 2.5 wt.%, indicating that the $CeO_2$ abrasives were approaching saturation in the dispersion. However, upon further increasing the $CeO_2$ concentration, the abrasives exceeded saturation, resulting in particle aggregation and sedimentation. This supersaturation led to a decrease in both the dispersion quality and the stability of the polishing solution.

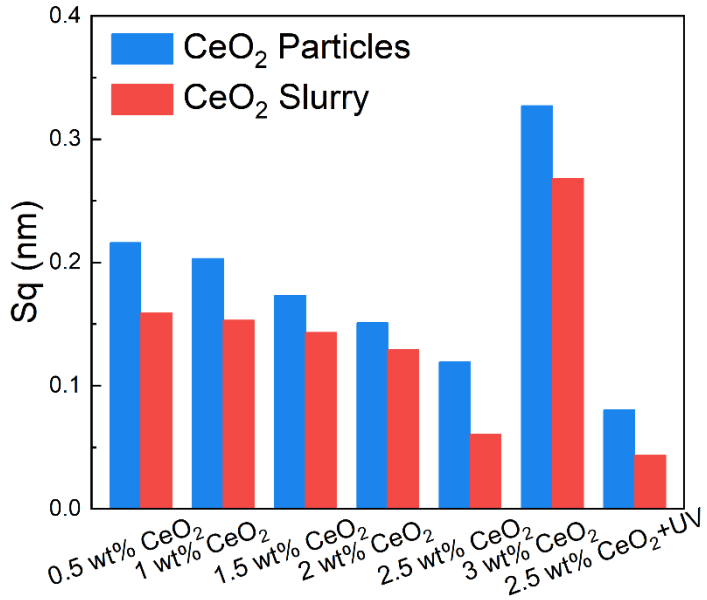


**Supplementary Fig. S11.** Sq comparison for $CeO_2$ particles and Janus $CeO_2$ slurry at various weight concentrations and UV illumination.

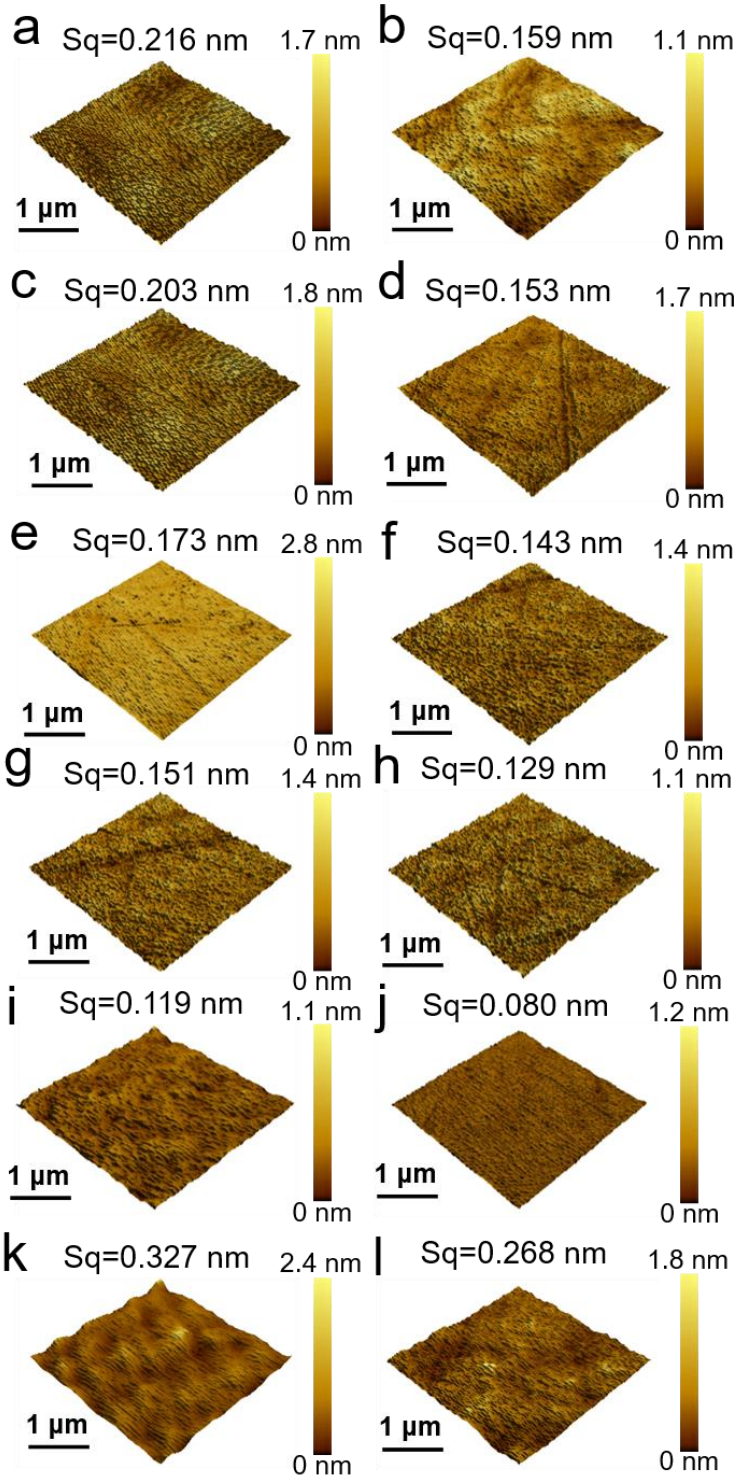


**Supplementary Fig. S12.** 3D AFM images of Si wafer surfaces polished under various weight concentrations $CeO_2$ particles and Janus $CeO_2$ slurry: **a** 0.5 wt% (particles); **b** 0.5 wt% (slurry); **c** 1 wt% (particles); **d** 1 wt% (slurry); **e** 1.5 wt% (particles); **f** 1.5 wt% (slurry); **g** 2 wt% (particles); **h** 2 wt% (slurry); **i** 2.5 wt% (particles); **j** 2.5 wt% (particles)+UV; **k** 3 wt% (particles); **l** 3 wt% (slurry).

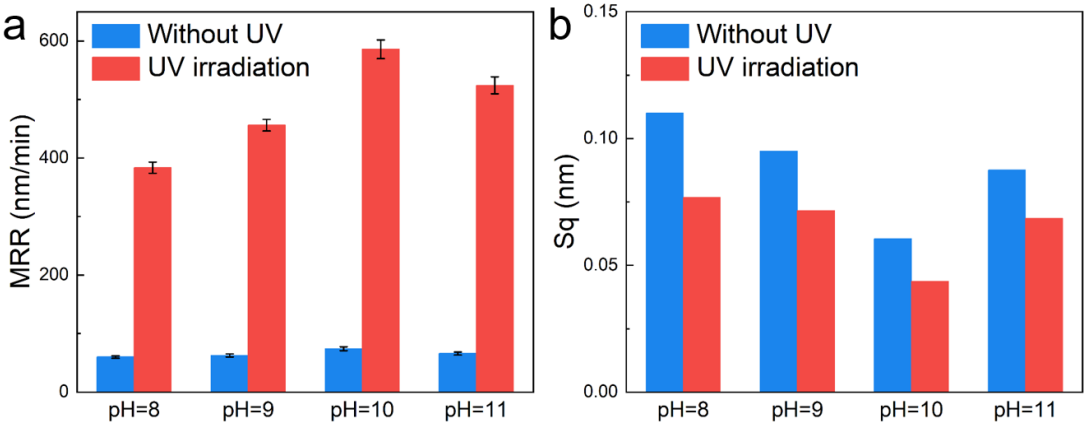


298 **Supplementary Fig. S13.** Comparison of **a** MRR, **b** Sq for Si wafers polished at

299 different pH levels.

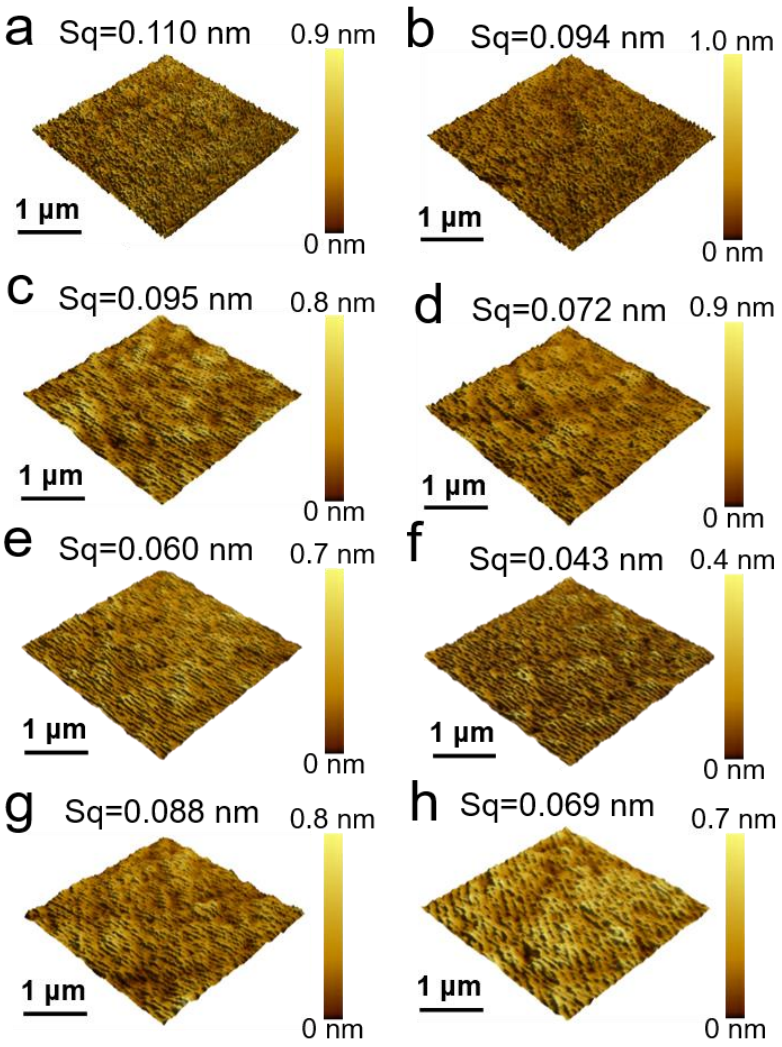


**Supplementary Fig. S14.** 3D AFM images of Si wafer surfaces polished under different pH: **a** pH=8; **b** pH=8 (UV); **c** pH=9; **d** pH=9 (UV); **e** pH=10; **f** pH=10 (UV); **g** pH=11; **h** pH=11 (UV).

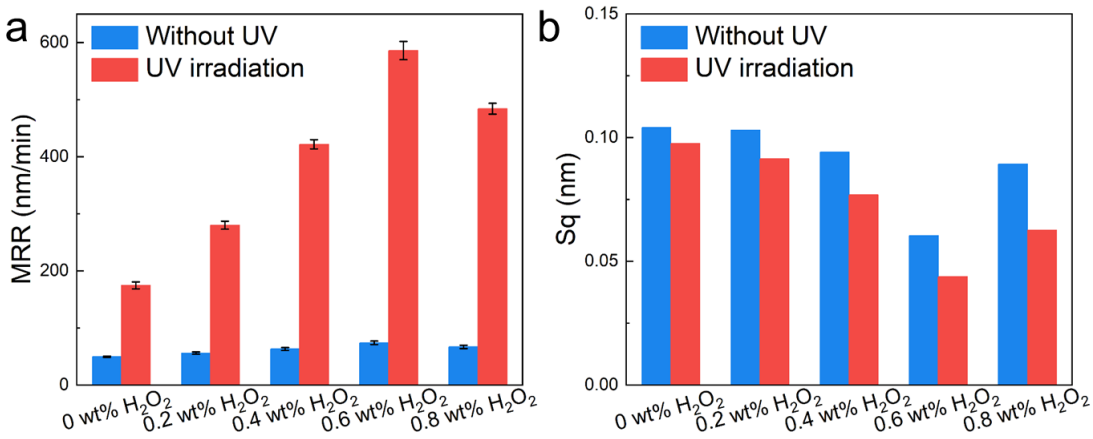


303 **Supplementary Fig. S15.** Comparison of **a** MRR, **b** Sq for the Si wafers polished
304 under different weight concentrations of $H_2O_2$.

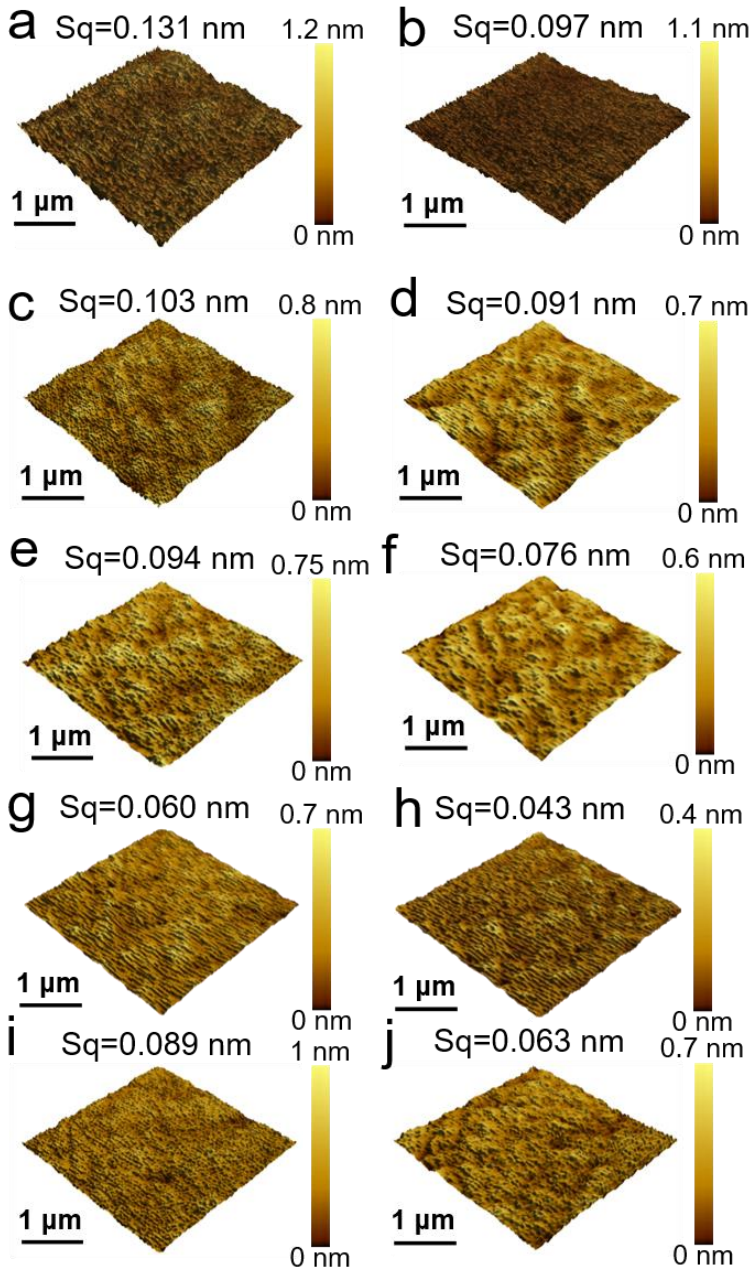


**Supplementary Fig. S16.** 3D AFM images of Si wafer surfaces polished under different weight concentrations of $H_2O_2$: **a** 0 wt%; **b** 0 wt% (UV); **c** 0.2 wt%; **d** 0.2 wt% (UV); **e** 0.4 wt%; **f** 0 .4wt% (UV); **g** 0.6 wt%; **h** 0.6 wt% (UV); **i** 0.8 wt%; **j** 0.8 wt% (UV).

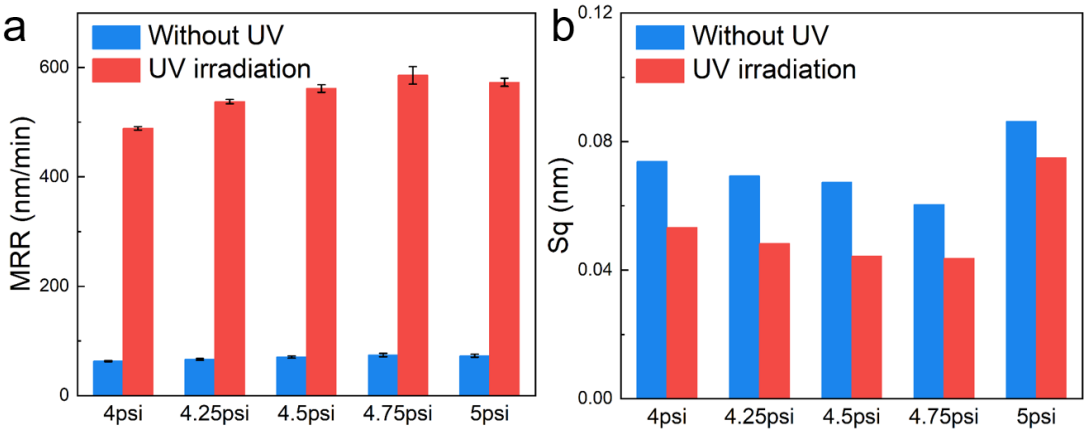


309 **Supplementary Fig. S17.** Comparison of **a** MRR, **b** Sq on the Si wafers polishing
310 under different polishing pressure.

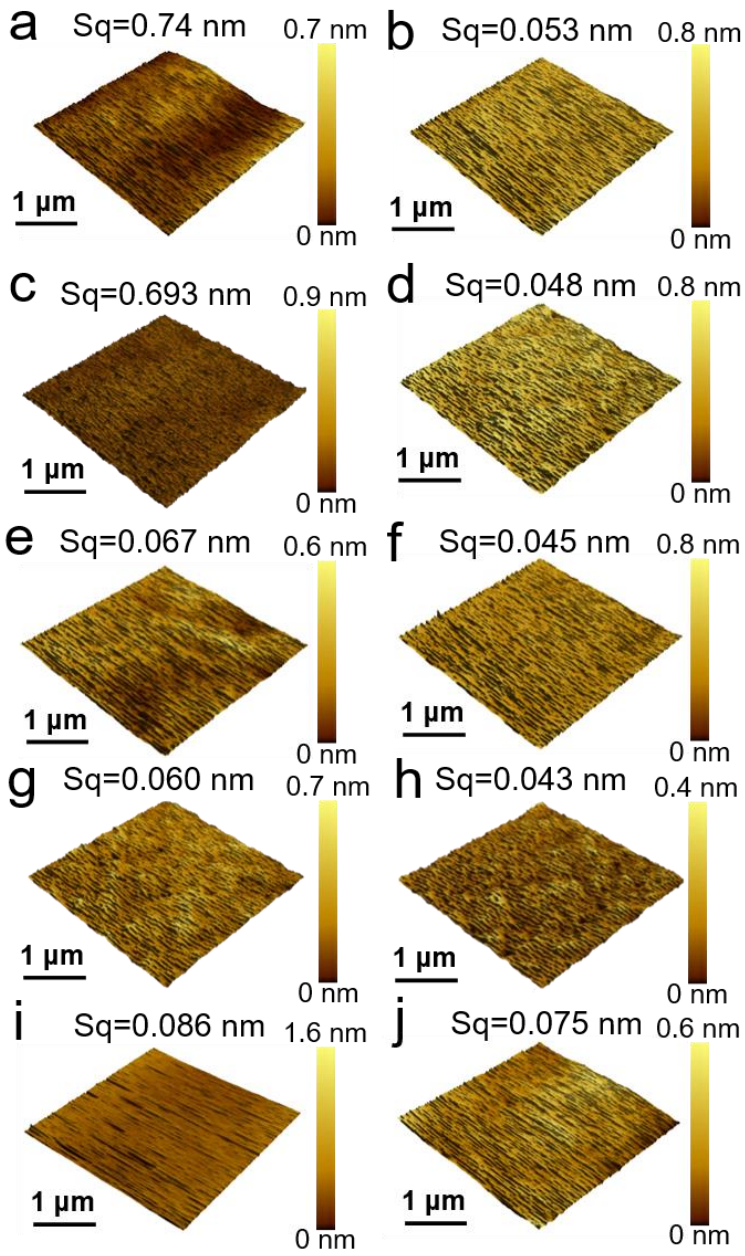


**Supplementary Fig. S18.** 3D AFM images of Si wafer surfaces polished under different polishing pressure: **a** 4 psi; **b** 4 psi (UV); **c** 4.25 psi; **d** 4.25 psi (UV); **e 4.**5 psi; **f** 4.5 psi (UV); **g** 4.75 psi; **h** 4.75 psi (UV); **i** 5 psi; **j** 5 psi (UV).

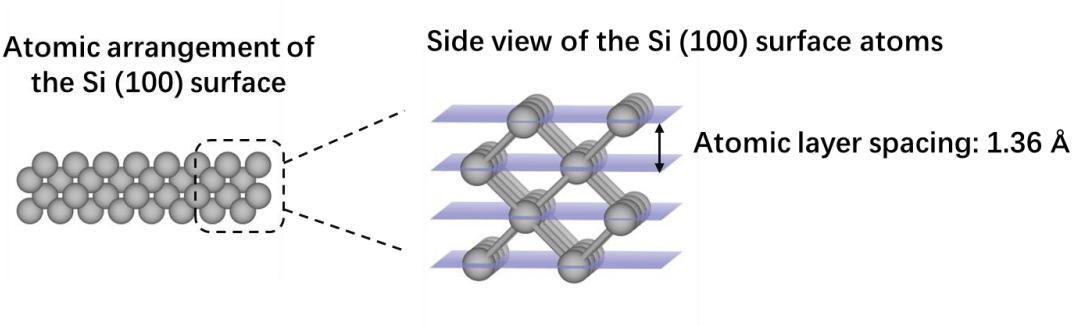


**Supplementary Fig. S19.** Atomic arrangement of the Si (100) surface.

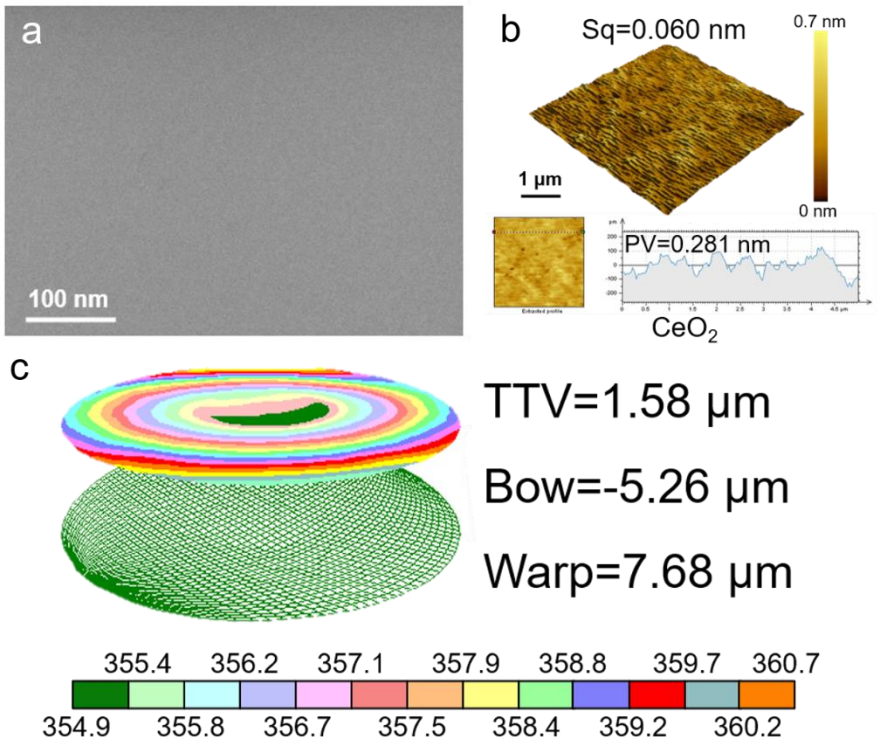


315 **Supplementary Fig. S20. a** 3D AFM image and height profiles. **b** SEM image. **c** Si

316 Geometric parameter image using Janus $CeO_2$ slurry (2.5 wt%).

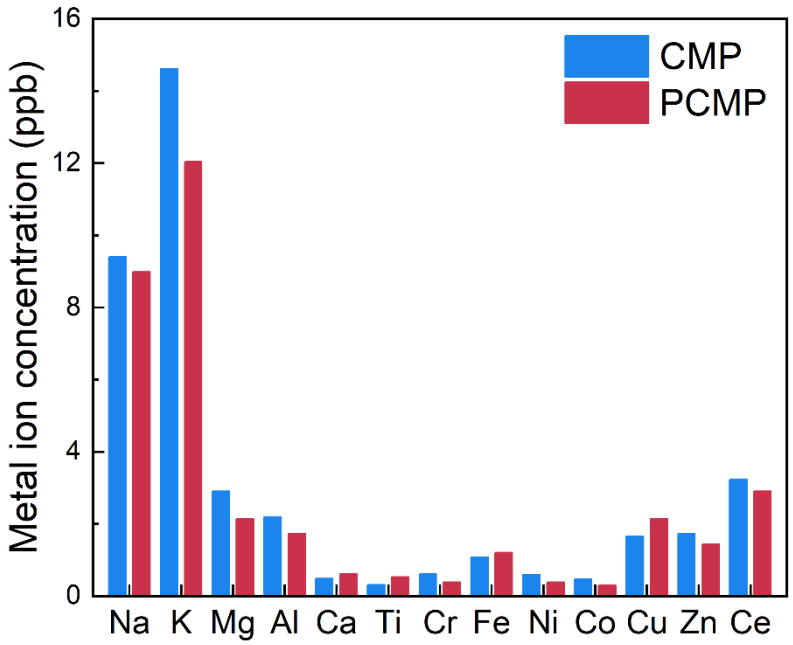


317 **Supplementary Fig. S21.** The polished Si wafers of metal element concentration.

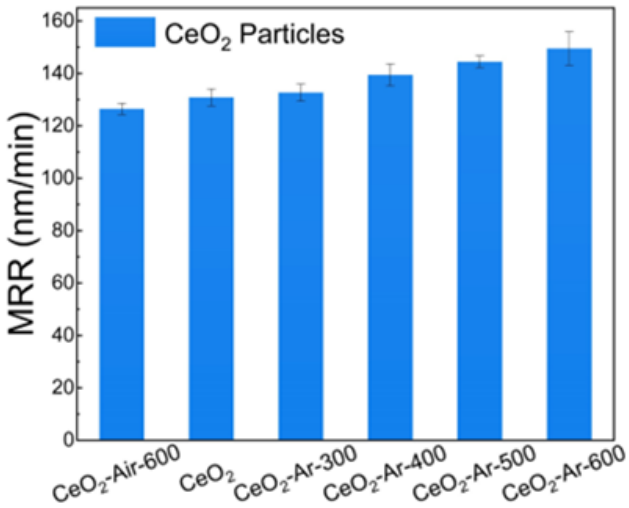


**Supplementary Fig. S22. a** Comparison of MRR on $SiO_2$ wafers with $CeO_2$ under different conditions.

**Discussion:** The MRR of $SiO_2$ during CMP using $CeO_2$ particles subjected to different calcination conditions was investigated. Samples calcined in air ($CeO_2$-Air-600) exhibited the lowest MRR, attributed to the reduced concentration of oxygen vacancies, as air calcination tends to replenish lattice oxygen. In contrast, $CeO_2$ samples calcined in an Ar atmosphere showed progressively higher MRRs with increasing calcination temperatures (300–600 °C), due to the enhanced formation of oxygen vacancies. These results indicate that oxygen vacancies in $CeO_2$ can improve its chemical reactivity, thereby promoting more efficient $SiO_2$ removal during CMP.

However, the formation of oxygen vacancies reaches a saturation point beyond which further increase becomes limited. Since the oxidation of the Si surface is the rate-determining step in the CMP process, boosting the oxidation rate can result in several-fold increases in MRR. In contrast, increasing oxygen vacancy concentration alone yields only marginal improvements.

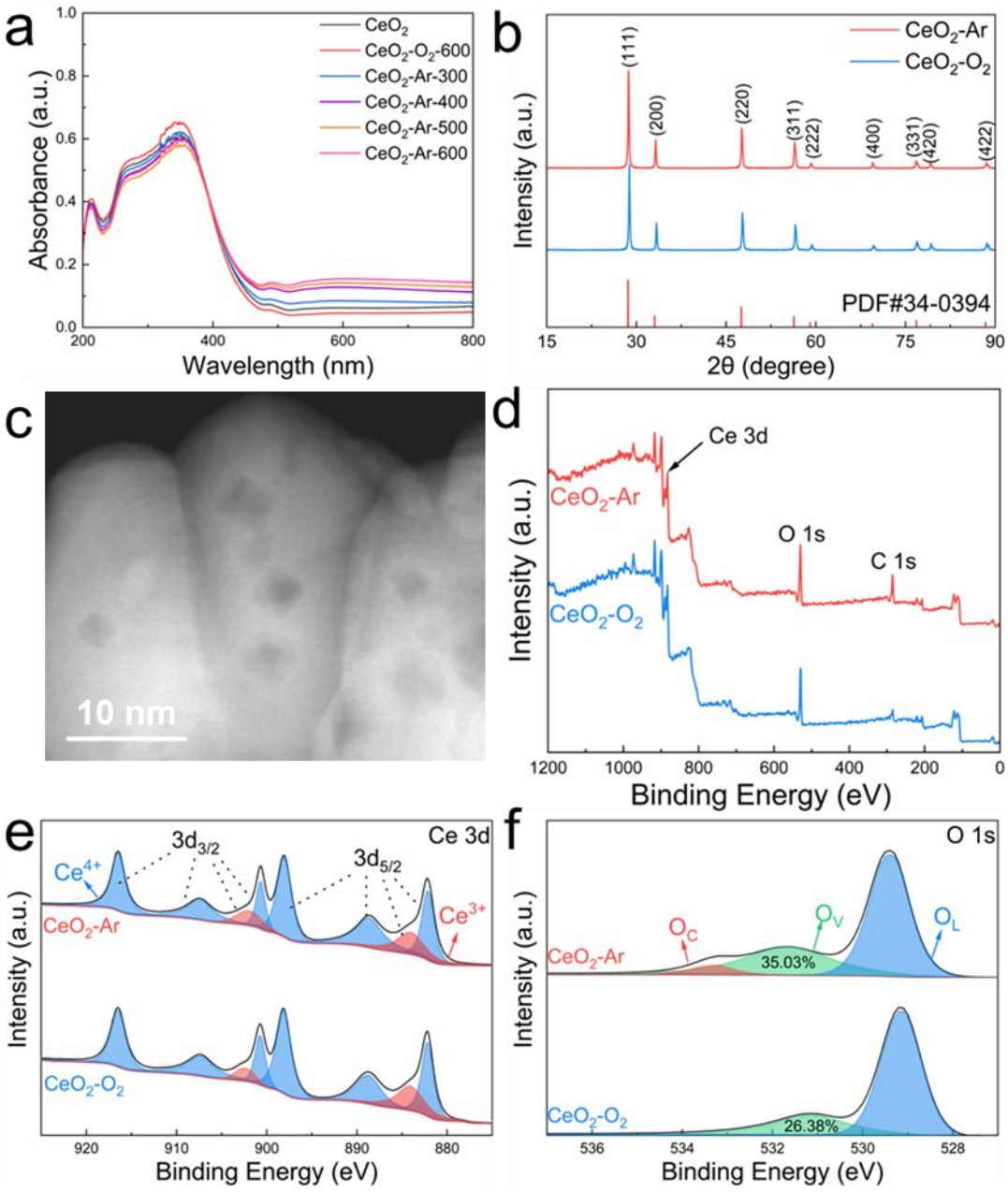


**Supplementary Fig. S23. a** UV-Vis spectra. **b** XRD pattern. c HAADF-STEM of $CeO_2$-Ar-600. **d** XPS spectra, **e** Ce 3d, **d** O 1s XPS spectra of $CeO_2$-Ar and $CeO_2$-$O_2$.

**Discussion:** Oxygen treatment tends to fill oxygen vacancies, while annealing in Ar atmosphere promotes oxygen diffusion out of the lattice, thereby generating oxygen vacancies. As shown in Fig. S23a, visible light absorption in the 500–800 nm range gradually increases with the

concentration of oxygen vacancies, suggesting enhanced defect-related electronic transitions.

XRD analysis (Fig. S23b) reveals a leftward shift of diffraction peaks in $CeO_2$ samples annealed under Ar ($CeO_2$–Ar) compared to those treated in $O_2$ ($CeO_2$–$O_2$), consistent with lattice expansion. This shift is attributed to two coupled effects: (1) the formation of oxygen vacancies, which locally disrupt the fluorite structure, and (2) the partial reduction of $Ce^{4+}$ to $Ce^{3+}$, whose larger ionic radius (1.14 Å for $Ce^{3+}$ vs. 0.97 Å for $Ce^{4+}$ in 8-fold coordination) leads to elongation of Ce–O bonds to preserve charge neutrality[7].

These structural modifications are further corroborated by HAADF-STEM and XPS (Fig. S23c–f). The HAADF-STEM image clearly displays abundant surface defects on $CeO_2$–Ar particles. XPS analysis of the O 1s spectra shows that the oxygen vacancy contribution increases from 26.38% in $CeO_2$–$O_2$ to 35.03% in $CeO_2$–Ar (Fig. S23f), validating the effectiveness of Ar annealing in enhancing defect concentration. Together, these results demonstrate a strong correlation between reduction state, lattice parameter, and oxygen vacancy concentration, highlighting the critical role of defect thermodynamics in tailoring the structural and electronic properties of ceria-based materials.

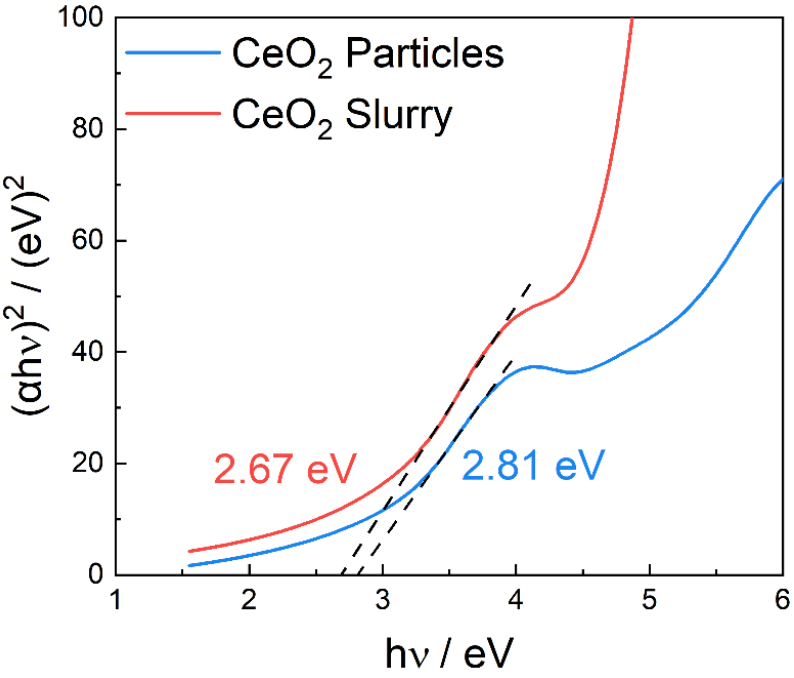


**Supplementary Fig. S24.** Tauc plot of $CeO_2$ particles and $CeO_2$ slurry.

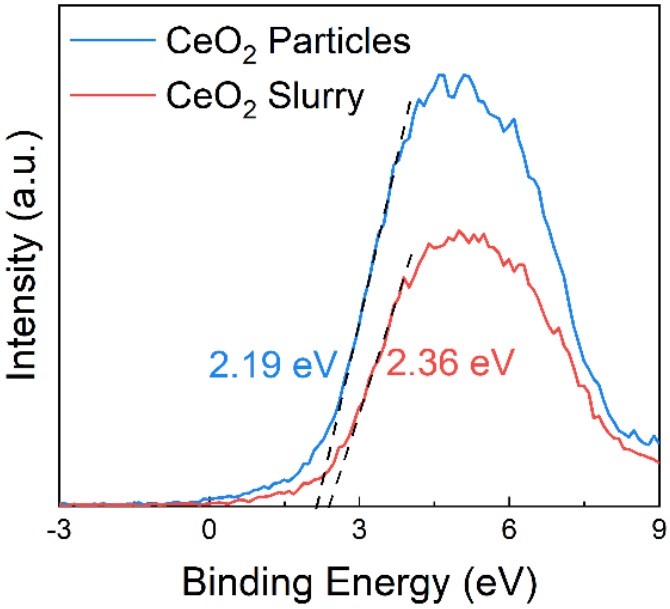


**Supplementary Fig. S25.** UPS valence band spectra of $CeO_2$ particals and slurry.

**Discussion:** The presence of oxygen vacancies causes electrons at the top of the valence band to shift to lower energy levels[8], resulting in valence band potentials of 2.36 eV for $CeO_2$ particles and 2.19 eV for Janus $CeO_2$ slurry.

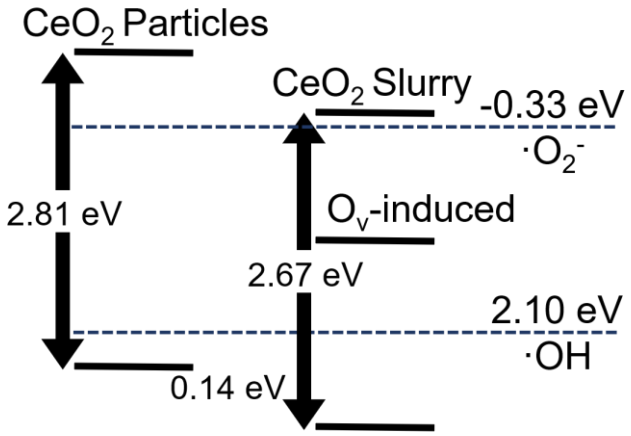


**Supplementary Fig. S26.** The band structure of $CeO_2$ particles and $CeO_2$ slurry.

**Discussion:** The constructed band structure reveals that the Janus $CeO_2$ slurry possesses a band gap of 2.67 eV, corresponding to an absorption edge of approximately 465 nm, which enables efficient excitation under 365 nm UV irradiation. Notably, the conduction band minimum (CBM) lies above the redox potential of $O_2/\cdot O_2^-$ (–0.33 V vs. NHE), while the valence band maximum (VBM) is below the redox potential of $H_2O/\cdot OH$ (+2.38 V vs. NHE). This favorable band alignment facilitates the generation of both superoxide ($\cdot O_2^-$) and hydroxyl (·OH) radicals upon photoexcitation. These reactive oxygen species contribute synergistically to the oxidative enhancement observed during the PCMP process.

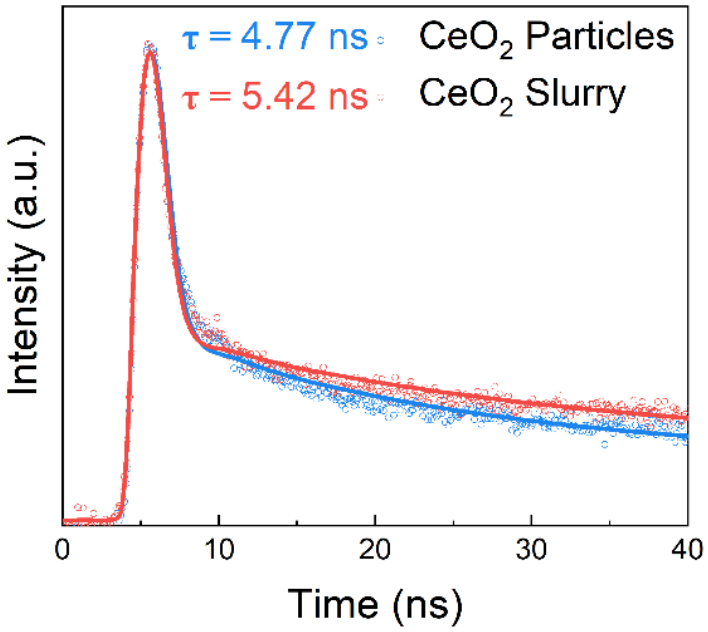


**Supplementary Fig. S27.** Time-resolved PL decay curves of $CeO_2$ particles and $CeO_2$ slurry.

**Discussion:** The transient fluorescence lifetimes of $CeO_2$ particles and Janus $CeO_2$ slurry are 4.77 ns and 5.42 ns, respectively. It indicates oxygen vacancies act as an electronic trap to induce local band structure changes in $CeO_2$, particularly forming mid-gap states in regions with oxygen deficiency[9, 10]. These mid-gap states act as intermediate trapping sites for electrons transitioning from the excited to the ground state, slowing the electron recombination pathway and thereby extending the lifetime of photo-generated charge carriers.

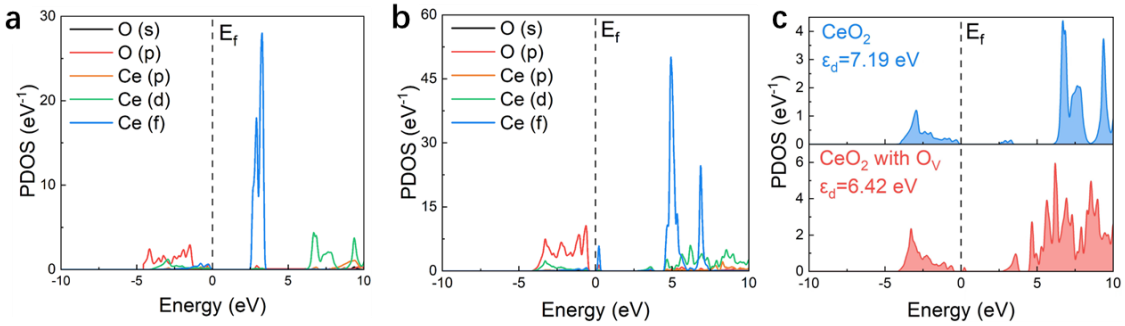


**Supplementary Fig. S28. a** Projected density of states of $CeO_2$. **b** $CeO_2$ with $O_V$. **c** Projected density of states of Ce 3d orbitals. The Fermi level is set to zero.

**Discussion:** The electronic structures of $CeO_2$ with and without oxygen vacancies were analyzed by partial density of states (PDOS) calculations. It reveals that oxygen vacancies lead to excess electrons occupying the Ce 4f states, creating new electronic states, and the excess electron gain by the 4f would give rise to the charge carrier in the band. Compared to $CeO_2$, the d-band center of $CeO_2$ with oxygen vacancy is closer to the 0.77 eV. Therefore, defect states cause band tailing and act as mid-states, enabling electrons to be excited from the valence band to the conduction band through multi-step excitation processes. This enhances the light utilization efficiency of $CeO_2$ and boosts the generation rate and lifetimes of photo-generated carriers.

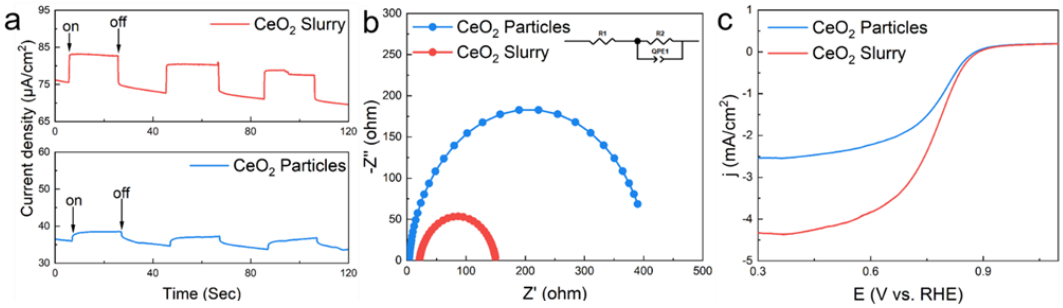


**Supplementary Fig. S29. a** Transient photocurrent response. **b** Polarization curves. **c** Nyquist plot of $CeO_2$ particles and $CeO_2$ slurry.

**Discussion:** The photocurrent densities over time under three cycles of intermittent illumination (Fig. S29a) demonstrated that $CeO_2$ particles exhibited weak current densities when illuminated, whereas the $CeO_2$ slurry produced a distinct photocurrent response. Upon switching off the Xe lamp, the photocurrent values of both samples rapidly declined. Notably, the photocurrent density of the $CeO_2$ slurry reached 7.55 $\mu A/cm^2$, which was 3.07 times higher than that of $CeO_2$ particles.

In the Nyquist plot (Fig. S29b), the semicircular radius for the $CeO_2$ slurry was smaller than that of $CeO_2$ particles, indicating lower charge transfer resistance. Additionally, the $CeO_2$ slurry displayed superior oxygen reduction reaction (ORR) performance in linear sweep voltammetry (LSV) measurements (Fig. S29c), with an onset potential of 0.87 V and a half-wave potential ($E_{1/2}$) of 0.81 V, outperforming the $CeO_2$ particles (0.77 V and 0.74 V, respectively). These results highlight the highly efficient photogenerated charge transport capabilities of the $CeO_2$ slurry compared to $CeO_2$ particles.

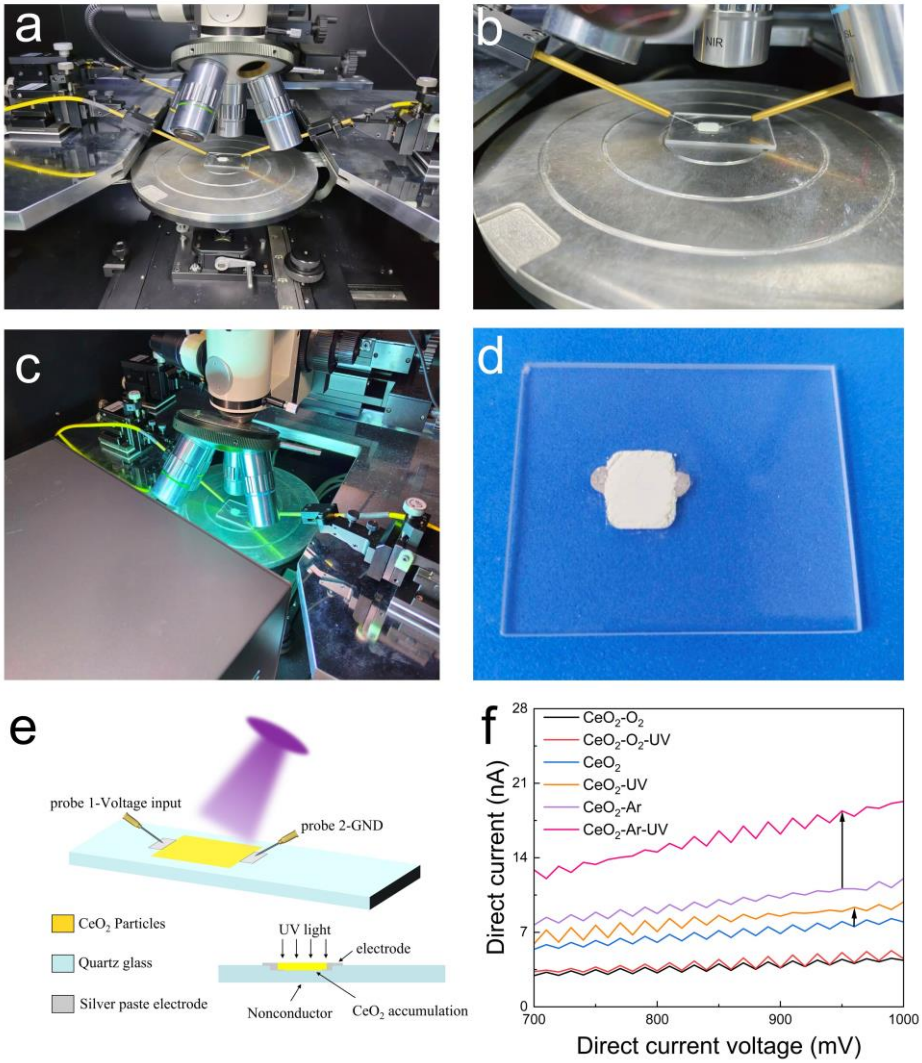


**Supplementary Fig. S30. a** Schematic illustration of the I-V sweep of electrochemical electrode. **b** Probe contacting. **c** Electrochemical measurements under UV light. **d** Electrode containing cerium dioxide particles. **e** Schematic illustration of the electrochemical electrode under UV irradiation. and f voltage sweep from 700 mV to 1000 mV of the electrode.

**Discussion:** The photoresponse behavior of various $CeO_2$ were evaluated under UV irradiation using a two-probe I–V measurement setup (Fig. S30a-e). The samples were deposited on quartz glass substrates with silver paste electrodes, and UV light was applied vertically to excite photo-generated carriers. As shown in Fig. S30f, the $CeO_2$ sample

calcined under an Ar atmosphere and subjected to UV irradiation ($CeO_2$–Ar–UV) exhibited the highest photocurrent among all samples. This enhanced photocurrent is attributed to the high concentration of oxygen vacancies, which introduce shallow defect levels within the band gap. These defect levels act as trapping centers for photo-generated electrons, reducing carrier recombination and facilitating charge separation and transport. Additionally, the localized states enable sub-bandgap excitation and improved conductivity under UV light. In contrast, $CeO_2$ calcined in an $O_2$ atmosphere exhibited much lower photocurrent, due to the fill of oxygen vacancies, which hinders the excitation and transport of photo-generated carriers.

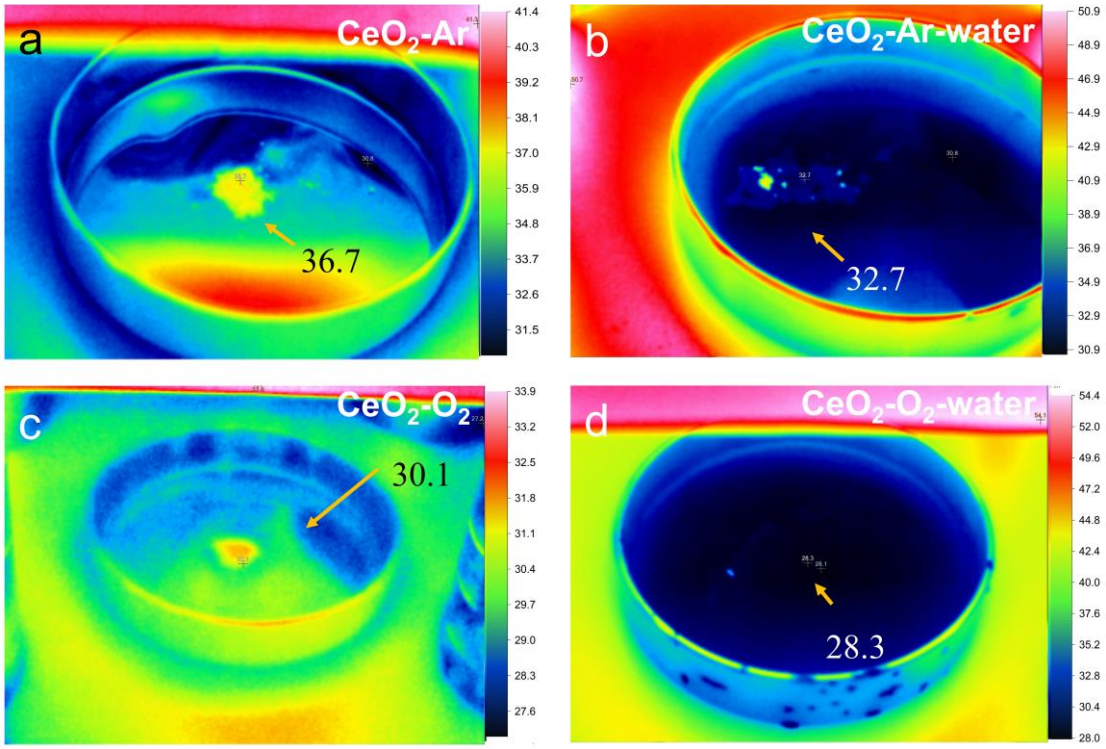


**Supplementary Fig. S31.** Infrared thermal images of $CeO_2$ samples under UV illumination. **a** $CeO_2$-Ar, **b** $CeO_2$-Ar-water, **c** $CeO_2$-$O_2$, and d $CeO_2$-$O_2$-water.

**Discussion:** The $CeO_2$–Ar sample exhibits the highest surface temperature (36.7 °C), attributed to the presence of abundant oxygen vacancies that promote non-radiative recombination and local heating. In contrast, $CeO_2$–$O_2$, with fewer oxygen vacancies, shows a significantly lower temperature (30.1 °C). The addition of water reduces the surface temperature due to its cooling and shielding effects, with $CeO_2$–$O_2$–water reaching the lowest temperature (28.3 °C). These results highlight the role of oxygen vacancies and medium composition in regulating photothermal behavior.

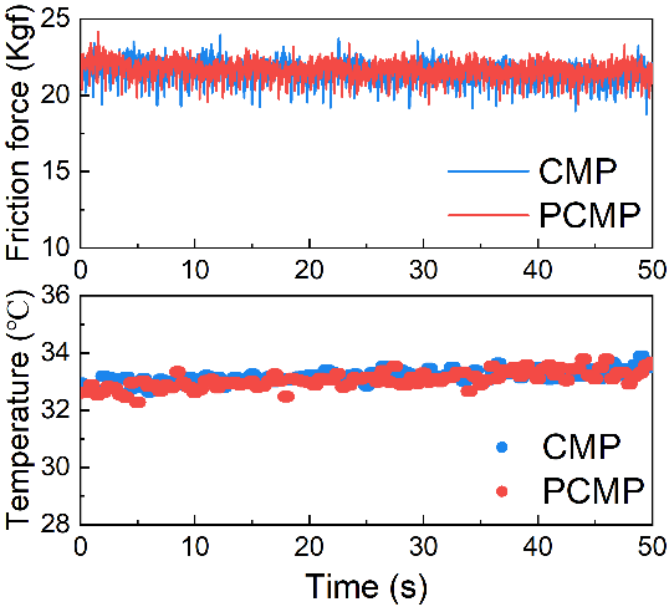


**Supplementary Fig. S32.** Friction force and slurry temperature during conventional CMP and PCMP.

**Discussion:** As shown in Fig. S32, the friction force and temperature remain relatively stable and comparable between CMP and PCMP, indicating similar polishing conditions. This is because the slurry is in dynamic flow during polishing, preventing heat accumulation in the bulk and limiting temperature rise to the $CeO_2$ surface. The localized heating of $CeO_2$ surface originates from non-radiative recombination of photo-generated carriers on the $CeO_2$ surface, which releases energy as phonons and elevates the temperature at the abrasive–wafer interface.

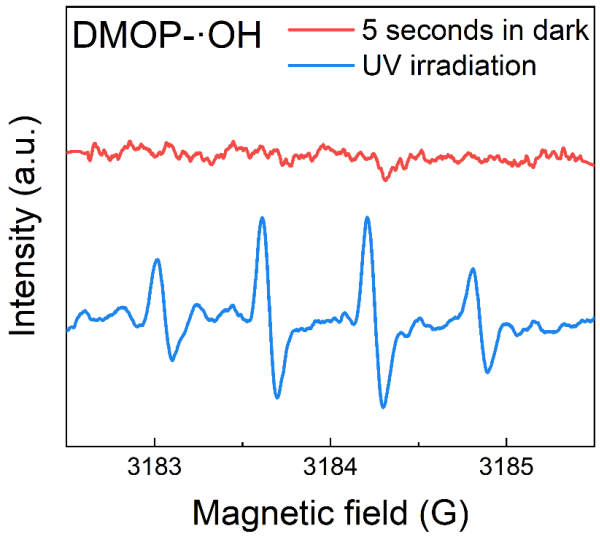


472 **Supplementary Fig. S33.** ESR spectra of DMPO-·OH for $CeO_2$ slurry under
473 different conditions.

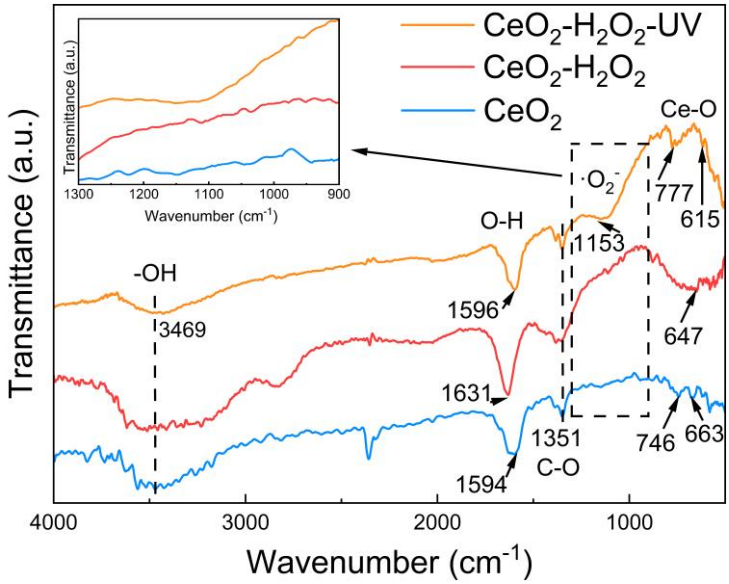


**Supplementary Fig. S34.** FTIR of $CeO_2$ under different conditions.

**Discussion:** A drop of $H_2O_2$ was added onto the pressed $CeO_2$ film, followed by UV irradiation after a 2-minute. Compared to pristine $CeO_2$, the $CeO_2$–$H_2O_2$ and $CeO_2$–$H_2O_2$–UV samples exhibit several new or enhanced peaks, indicating chemical interactions between $CeO_2$ and $H_2O_2$. The broad absorption band around 3469 $cm^{-1}$ is assigned to –OH stretching vibrations, while peaks near 1631 $cm^{-1}$ and 1596 $cm^{-1}$ correspond to O–H bending modes. A prominent peak at 1351 $cm^{-1}$ is attributed to C–O stretching. After UV irradiation, a new band appears at 1153 $cm^{-1}$, which is assigned to the formation of superoxide species on the $CeO_2$ surface. The Ce–O lattice vibrations are observed in the lower wavenumber region (900–500 $cm^{-1}$), with shifts from 663 $cm^{-1}$ and 746 $cm^{-1}$ to 647 $cm^{-1}$ and 777 $cm^{-1}$ in the UV-treated sample, suggesting lattice distortion and defect formation. The inset highlights the enhancement in the 900–1300 $cm^{-1}$ region, further confirming the generation of reactive oxygen species[11].

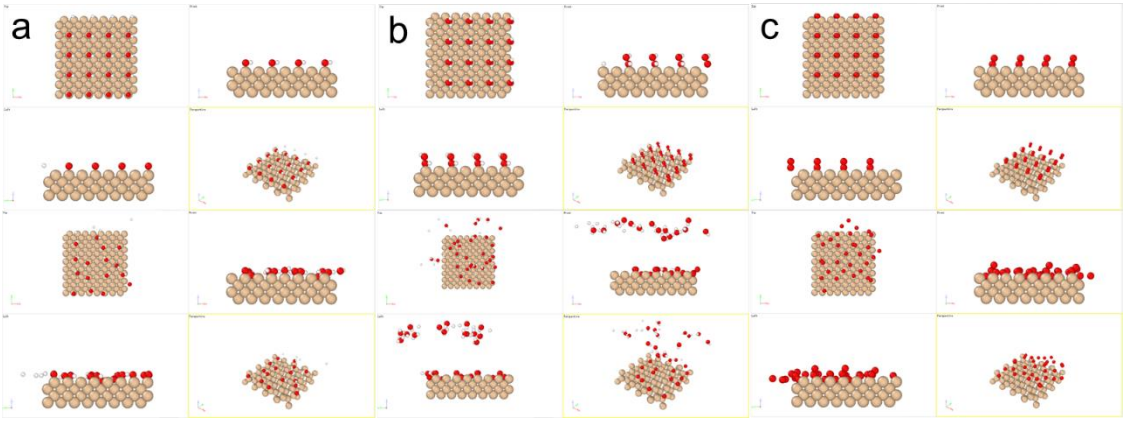


491 **Supplementary Fig. S35.** Molecular dynamic simulation of silicon oxidation with

492 (a) ·OH, (b) $H_2O_2$, and (c) $\cdot O_2^-$, with a molecular number of 16.

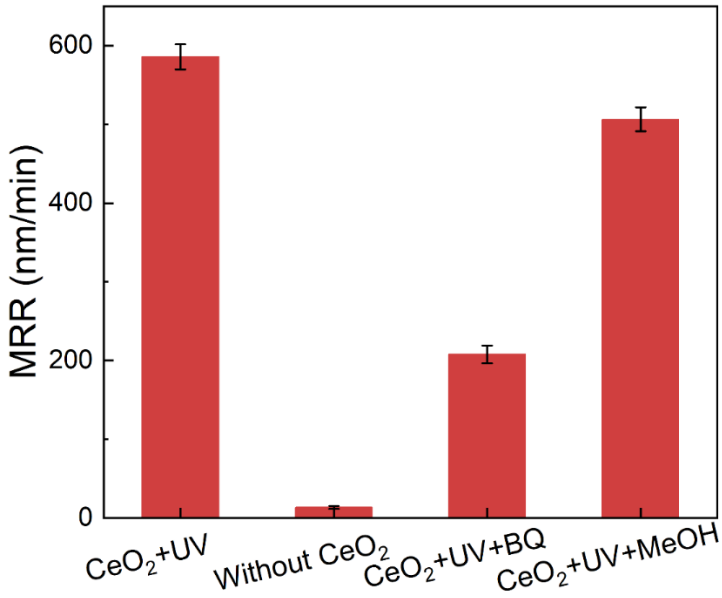


493 **Supplementary Fig. S36.** Comparison of MRR on Si wafers with different sacrificial

494 agents under polishing conditions.

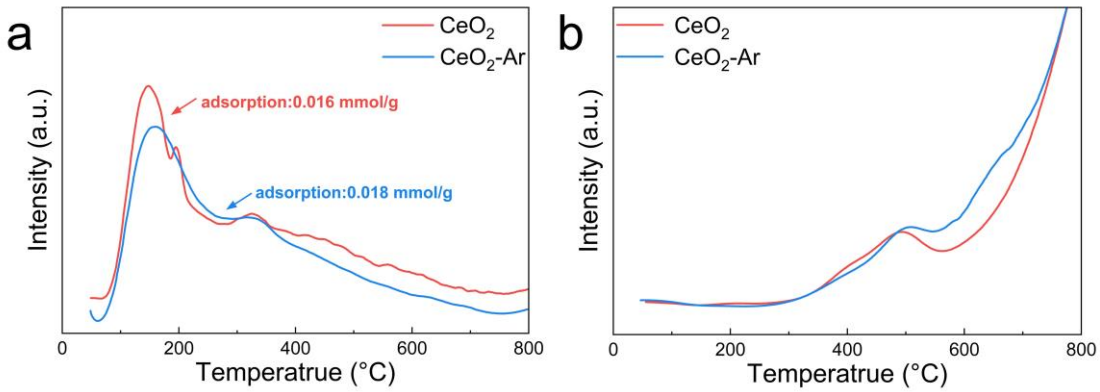


**Supplementary Fig. S37.** (a) $O_2$-TPD profiles of $CeO_2$, $CeO_2$-Ar-600 showing the adsorption amounts and strength of $O_2$. (b) $H_2$-TPR profiles of $CeO_2$ materials showing the reducibility of reactive SOS.

**Discussion:** Since TPD and TPR measurements require pretreatment to remove surface contaminants, and the Janus $CeO_2$ slurry contains organic components such as surfactants, which can interfere with the evaluation of oxygen vacancy adsorption and desorption behavior, Ar-calcined $CeO_2$ was used for characterization. Surface oxygen species on oxide nanomaterials include surface lattice oxygen atoms as well as adsorbed reactive oxygen species such as $*O_2$, $*O_2^-$, and $*O_2^{2-}$. The influence of enhanced defect states on $O_2$ adsorption and activation was investigated using $O_2$-temperature programmed desorption ($O_2$-TPD), which identifies the types and strengths of oxygen adsorption. For $CeO_2$ particles, desorption of $O_2$ between 50–200 °C is attributed to weakly adsorbed $*O_2^-$, while $*O_2$ desorbs between 150–300 °C[12]. As shown in Fig. S37a, compared to $CeO_2$, oxygen-deficient $CeO_2$ exhibits weaker physical adsorption but stronger chemical adsorption between 50–250 °C, based on acidity comparisons[13]. Fig. S37b further demonstrates that $CeO_2$ with oxygen vacancies possesses a higher $O_2$ storage capacity, consistent with the higher values of kinetic constants $k_2$ and $k_3$, facilitating the subsequent formation of superoxide radicals. Additionally, the desorption

curve at elevated reduction temperatures indicates that $CeO_2$-Ar-600 retains the oxidation capability associated with surface oxygen species.

$$Ce^{4+}+O_2^{-}\rightarrow Ce^{3+}+O_2 \qquad k_2 \qquad (1)$$

$$Ce^{3+}+O_2^{-}+2H^{+}\rightarrow Ce^{4+}+H_2O_2 \qquad k_3 \qquad (2)$$

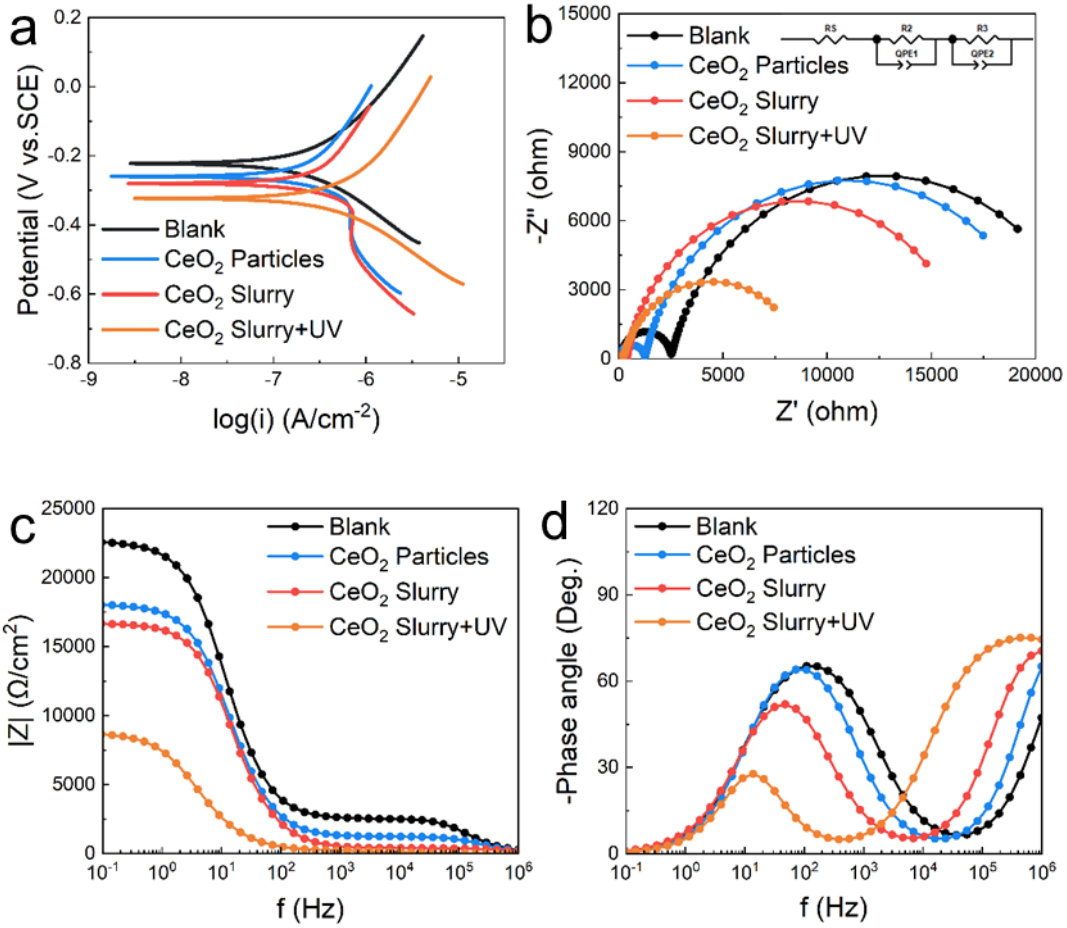


**Supplementary Fig. S38. a** Potential polarization plots of Si electrodes in the electrolytes under different conditions. **b** Nyquist for different electrolyte conditions, with the equivalent circuit models. **c** Bode-magnitude graphs. **d** Bode-phase graphs for different conditions. Post-immersion in solutions at pH 10.

**Discussion:** To further explore the contributions of various slurry components and the influence of UV light, the oxidation processes of the Si surface were systematically analyzed using potential dynamic polarization curves (Fig. S38a). The corrosion potential ($E_{corr}$) is the open-circuit potential at which the anodic (oxidation) and cathodic (reduction) reactions on a surface are balanced under steady-state conditions. A more negative $E_{corr}$ indicates a higher tendency for the material to oxidize, meaning it is more prone to corrosion. The corrosion

current density ($I_{corr}$) quantifies the rate at which corrosion proceeds. It is determined from the Tafel extrapolation of the polarization curve and is directly proportional to the corrosion rate. A higher $I_{corr}$ means a faster corrosion rate, indicating that the material is undergoing more rapid electrochemical degradation[14].

The $E_{corr}$ and $I_{corr}$, derived from Tafel plots, are summarized in Table S3. In the dispersed system of $CeO_2$ particles, the self-catalytic reaction requires significant interfacial pressure for initiation, resulting in an $E_{corr}$ of -0.222 V and $I_{corr}$ of $6.561 \times 10^{-7}$ A/cm². With the successive addition of slurry components and the introduction of UV light, $E_{corr}$ and $I_{corr}$ progressively increased, eventually reaching -0.323 V and $2.067 \times 10^{-6}$ A/cm². This progressive increase reflects the intensification of UV-induced photocatalytic reactions, which significantly accelerate the oxidation of the Si wafer.

Electrochemical Impedance Spectroscopy (EIS) can probe the interfacial properties of materials by applying a small-amplitude AC voltage over a wide range of frequencies and measuring the resulting current. To further understand the interfacial dynamics, EIS parameters were analyzed using a fitted equivalent circuit model (Fig. S38b), with impedance values compiled in Table S4. The interfacial charge transfer resistance decreased through the interaction between UV light and $CeO_2$, reaching R1 = 215 $\Omega \cdot cm^2$. This reduction could be attributed to generating electron-hole pairs that altered the ionic distribution at the interface between $CeO_2$ slurry and Si wafer under UV illumination, thereby enhancing the double-layer capacitance (QPE1) to $2.923 \times 10^{-8}$ $nF/cm^2$. The increased capacitance decreased the low-frequency impedance, highlighting the improved interfacial charge transfer between $CeO_2$ and Si.

The amplitude and phase Bode plots further corroborate this trend. Upon introducing UV light, the amplitude Bode plot (Fig. S38c) demonstrated a marked decrease in impedance modulus (|Z|) within the low-frequency region, suggesting a reduction in charge transfer resistance ($R_{ct}$). The phase Bode plot (Fig. S38d) exhibited minimal changes in the high-frequency region, predominantly influenced by the double-layer capacitance ($C_{dl}$). However, the phase angle decreased noticeably in the mid-to-low frequency range, indicating a transition from capacitive behavior to enhanced oxidation activity for the Si wafer.

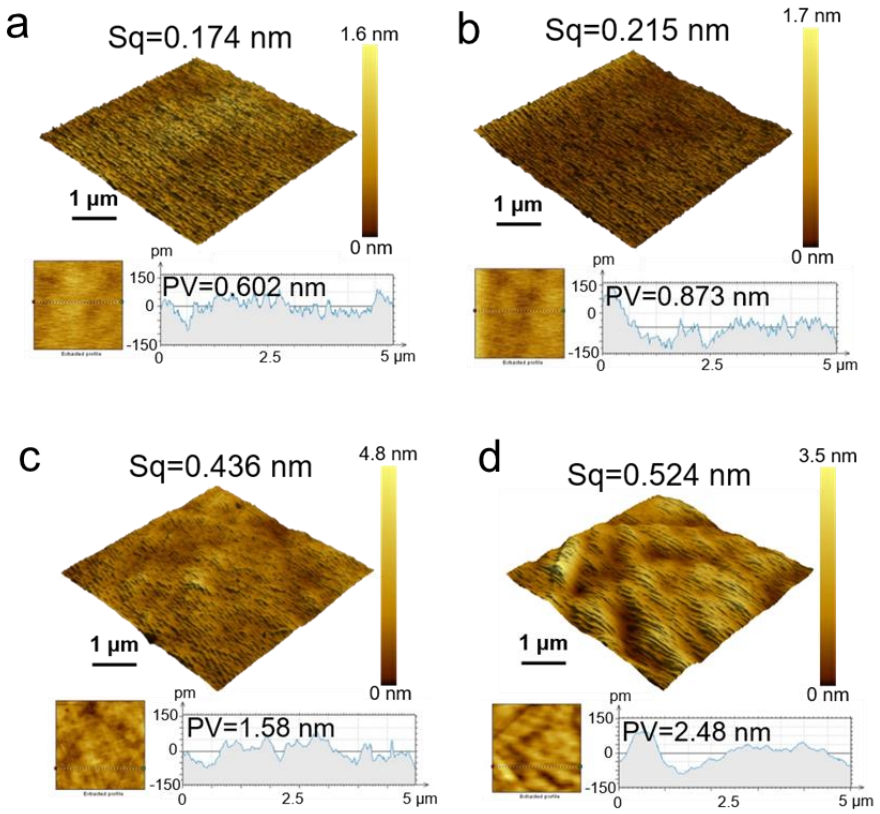


**Supplementary Fig. S39.** The 3D AFM images with corresponding height profiles for **a** Si wafer before immersion, **b** $CeO_2$ particles, **c** $CeO_2$ slurry, and **d** $CeO_2$ slurry with UV illumination.

**Discussion:** AFM investigations visually supported the oxidation processes. The Sq of the initial Si wafer was measured at 0.174 nm, with a PV of 0.602 nm, indicating a relatively smooth Si surface with minimal evidence of corrosion or surface alteration (Fig. S39a). With the progressive introduction of $CeO_2$ particles, slurry components, and UV light, the Sq increased gradually, reaching a final value of 0.524 nm, and the peak-to-valley height reached 2.48 nm (Fig. S39b-d).

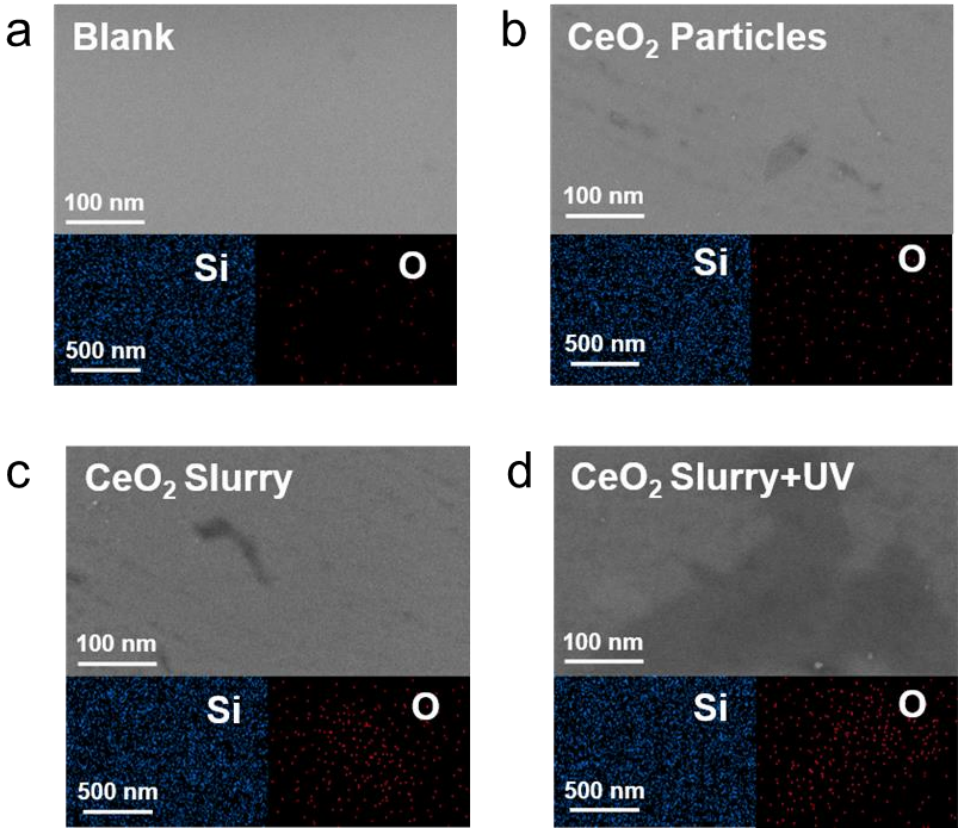


582 **Supplementary Fig. S40.** The SEM images, and EDS elemental mapping for Si and
583 O are shown for **a** Si wafer before immersion, **b** $CeO_2$ particles, **c** $CeO_2$ slurry, and **d**
584 $CeO_2$ slurry with UV illumination.

585

586 **Discussion:** SEM analyses further confirmed the formation of an
587 oxidation layer (Fig. S40), with elemental mapping showing a significant
588 increase in oxygen content (Table S5). Compared to the blank sample, the
589 oxygen content (both in weight and atomic percentages) increases
590 progressively with the addition of $CeO_2$ particles, $CeO_2$ slurry, and $CeO_2$
591 slurry under UV irradiation. Specifically, the atomic percentage of
592 oxygen increases from 3.31% (blank) to 14.69% ($CeO_2$ slurry + UV),
593 indicating a substantial enhancement in surface oxidation.

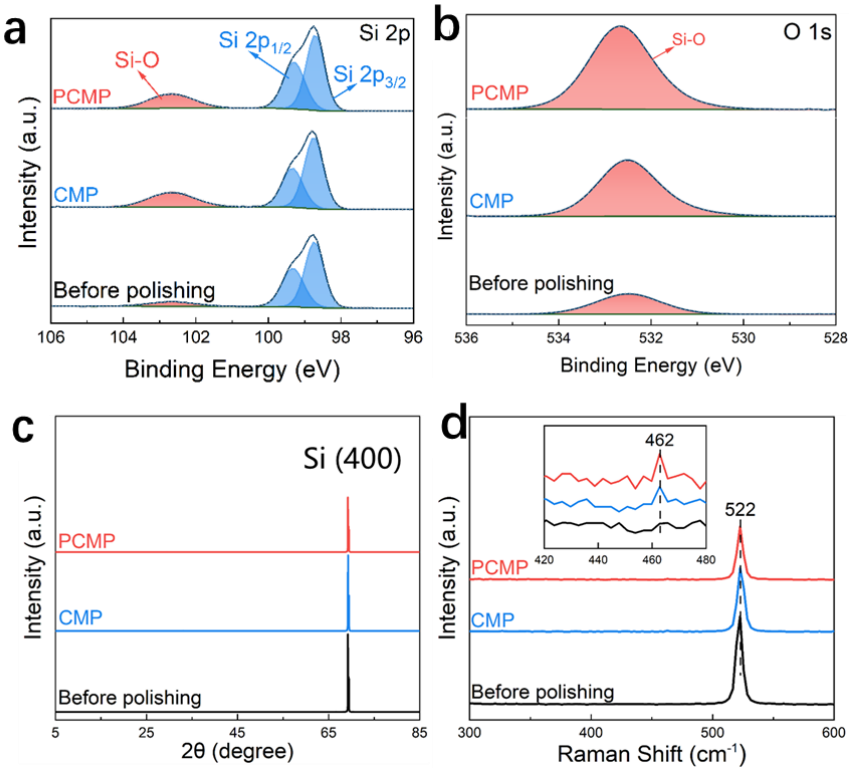


**Supplementary Fig. S41. a** Si 2p, **b** O 1s XPS spectra of Si wafers surface under different conditions. **c** XRD spectra. **d** Raman spectra of Si wafers surface under different conditions.

**Discussion:** XPS was conducted on Si wafers after CMP, and after PCMP to evaluate the surface oxygen content. In the Si 2p spectra (Fig. S41a), peaks at 98.70 eV and 99.30 eV were attributed to monocrystalline Si. In contrast, peaks at 102.58 eV in the Si 2p and 531.78 eV in the O 1s spectra (Fig. S41b) were attributed to Si-O bonds, confirming the oxidation processes during CMP and PCMP.

XRD patterns of the Si surface before polishing, after CMP, and after PCMP show a single diffraction peak at 69.63° corresponding to the Si (400) plane, with no additional peaks observed for $SiO_2$. This absence is attributed to the extremely thin and poorly crystalline nature of the surface oxide layer, making it undetectable by XRD (Fig. S41c). In contrast, Raman spectroscopy reveals a clear signal at 462 $cm^{-1}$ attributed

to the symmetric stretching vibration of the Si-O-Si bond, corresponding to the vibrational mode of amorphous silicon oxide (Fig. S41d). This peak is especially evident after PCMP treatment, indicating the formation of an oxide layer. The intensity ratio of the $SiO_2$ layer to monocrystalline silicon after CMP is 0.0237. In contrast, this ratio increases to 0.0363 after photocatalytic CMP, suggesting increased $SiO_2$ layer thickness.

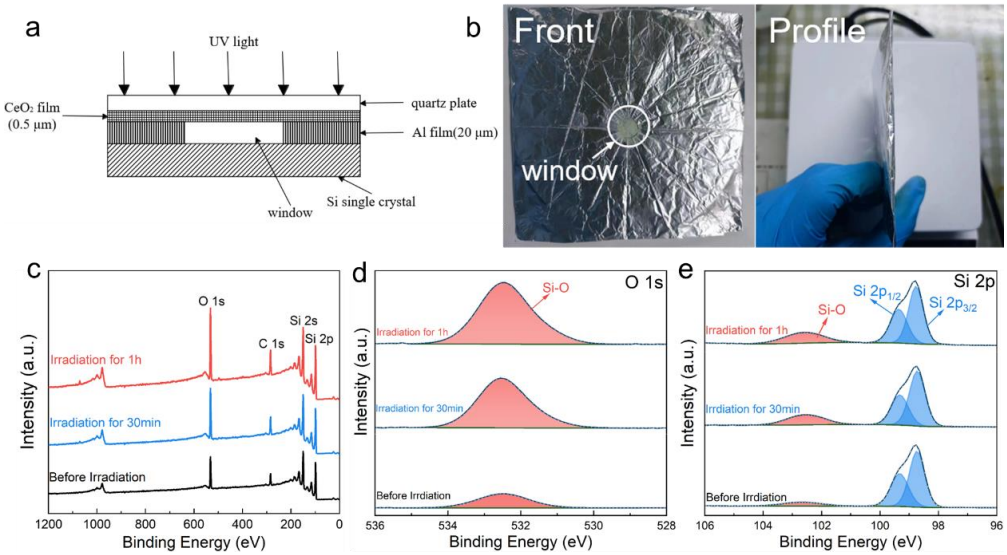


**Supplementary Fig. S42. a** Schematic illustration of the noncontact photocatalytic oxidation system for the Si wafer surface. **b** Digital image of the noncontact photocatalytic oxidation. **c** XPS spectra, **d** O 1s XPS spectra. **e** Si 2p XPS spectra of Si wafer surface under different radiation times.

**Discussion:** An aluminum metal film, approximately 20 μm thick, was placed between the quartz plate coated with the $CeO_2$ film and the Si substrate to maintain a gap distance of 20 μm between the $CeO_2$ film and the Si surface, ensuring noncontact conditions[15].

XPS spectra of the Si surface after irradiation for 0 h, 0.5 h, and 1 h demonstrated that $SiO_2$ formation could occur on the Si surface via photocatalytic oxidation even without direct contact between the $CeO_2$ film and the Si surface. The peaks at 532.40 and 532.20 eV binding energies in the O 1s XPS spectrum correspond to $SiO_2$ and Si-O, respectively. In the Si 2p XPS spectrum, the peaks at 98.70 and 99.30 eV are attributed to Si, while the peaks at 103.30 and 102.40 eV correspond to $SiO_2$ and Si-O, respectively. These results indicate that, even under noncontact conditions, the Si surface undergoes oxidation to form $SiO_2$ via photocatalytic activity from $CeO_2$, with longer irradiation times resulting in a more pronounced oxidation effect.

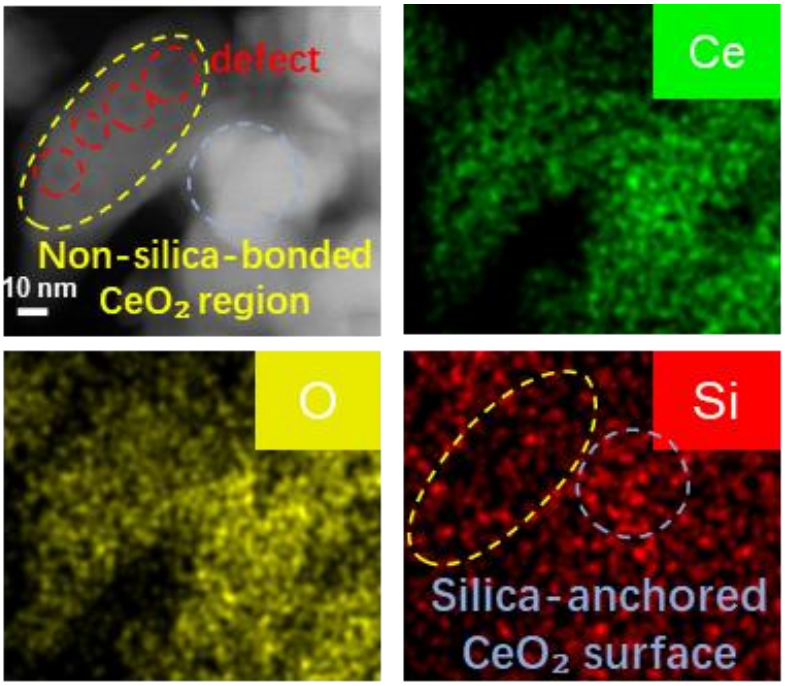


**Supplementary Fig. S43.** HAADF-STEM image and corresponding EDS elemental mappings of Ce (green), O (yellow), and Si (red) for $CeO_2$ particles after polishing a silicon wafer.

**Discussion:** To elucidate the interfacial interactions between $CeO_2$ abrasives and the silicon wafer during PCMP, HAADF-STEM and EDS mapping were performed on $CeO_2$ after polishing. The yellow dashed region marks a $CeO_2$ domain not bonded to silica, characterized by apparent structural defects. In contrast, the blue dashed region shows a silica-anchored $CeO_2$ surface, where strong co-localization of Ce, O, and Si signals suggests the formation of interfacial Ce–O–Si bonding.

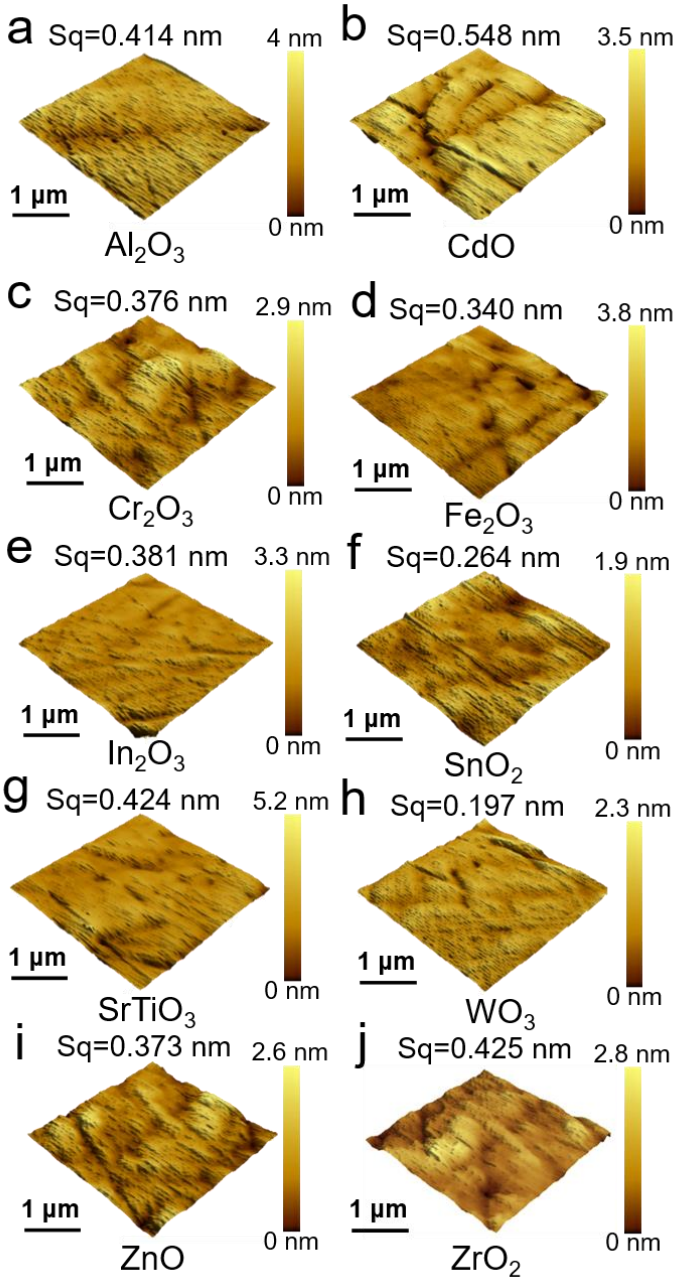


**Supplementary Fig. S44.** 3D AFM images of Si wafer surfaces polished under different abrasives: **a** $Al_2O_3$; **b** CdO; **c** $Cr_2O_3$; **d** $Fe_2O_3$; **e** $In_2O_3$; **f** $SnO_2$; **g** $SrTiO_3$; **h** $WO_3$; **i** ZnO; **j** $ZrO_2$.

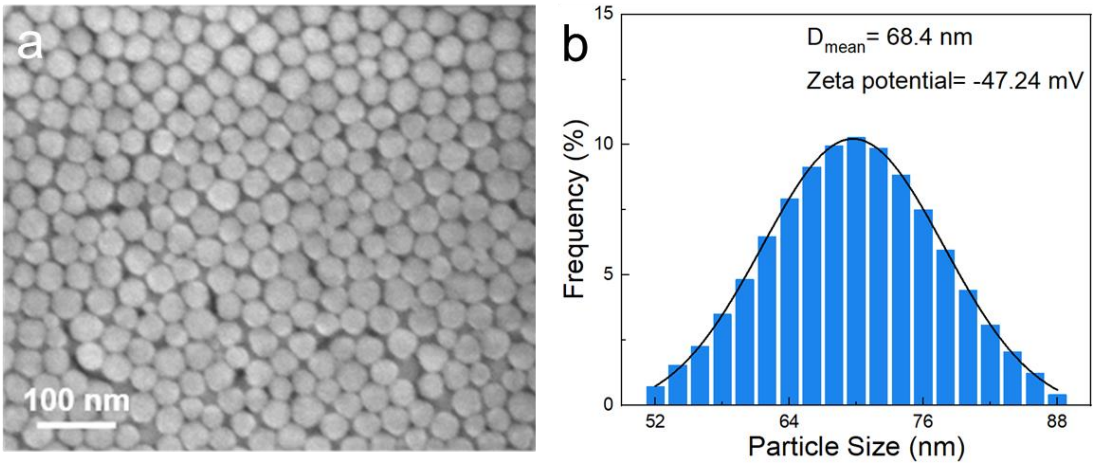


**Supplementary Fig. S45. a** SEM image of nano $SiO_2$. **b** Particle size distribution histogram and zeta potential of 2.5 wt.% $SiO_2$ exhibits an average $SiO_2$ particle size of 68.4 nm and a zeta potential of -47.24 mV.

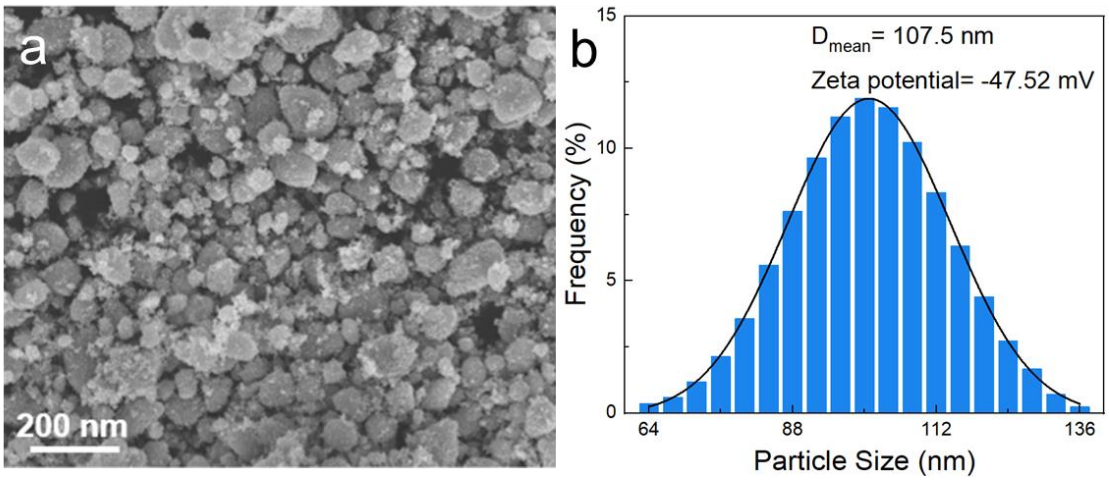


**Supplementary Fig. S46. a** SEM image of nano $TiO_2$. **b** Particle size distribution histogram and zeta potential of 2.5 wt.% $TiO_2$ exhibits an average $TiO_2$ particle size of 107.5 nm and a zeta potential of -47.52 mV.

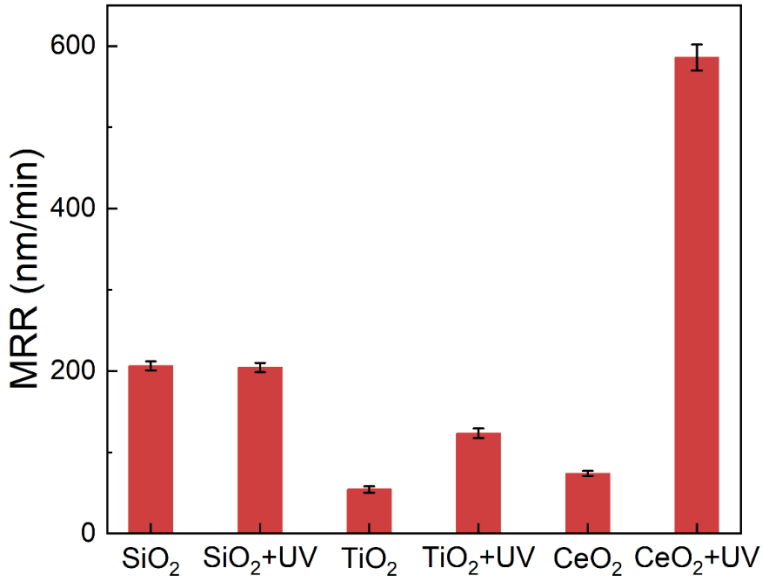


**Supplementary Fig. S47.** Comparison of MRR on the Si wafers by different slurries ($SiO_2$, $TiO_2$, $CeO_2$) containing 2.5 wt% $H_2O_2$ under various conditions of UV light at pH 10.

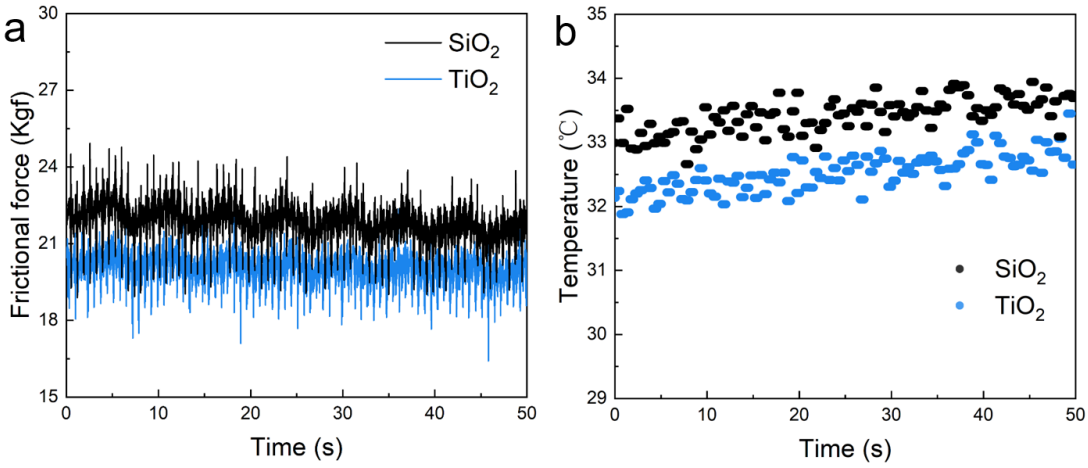


659 **Supplementary Fig. S48. a** Surface friction force. **b** Temperature of abrasives in
660 polishing Si wafers.

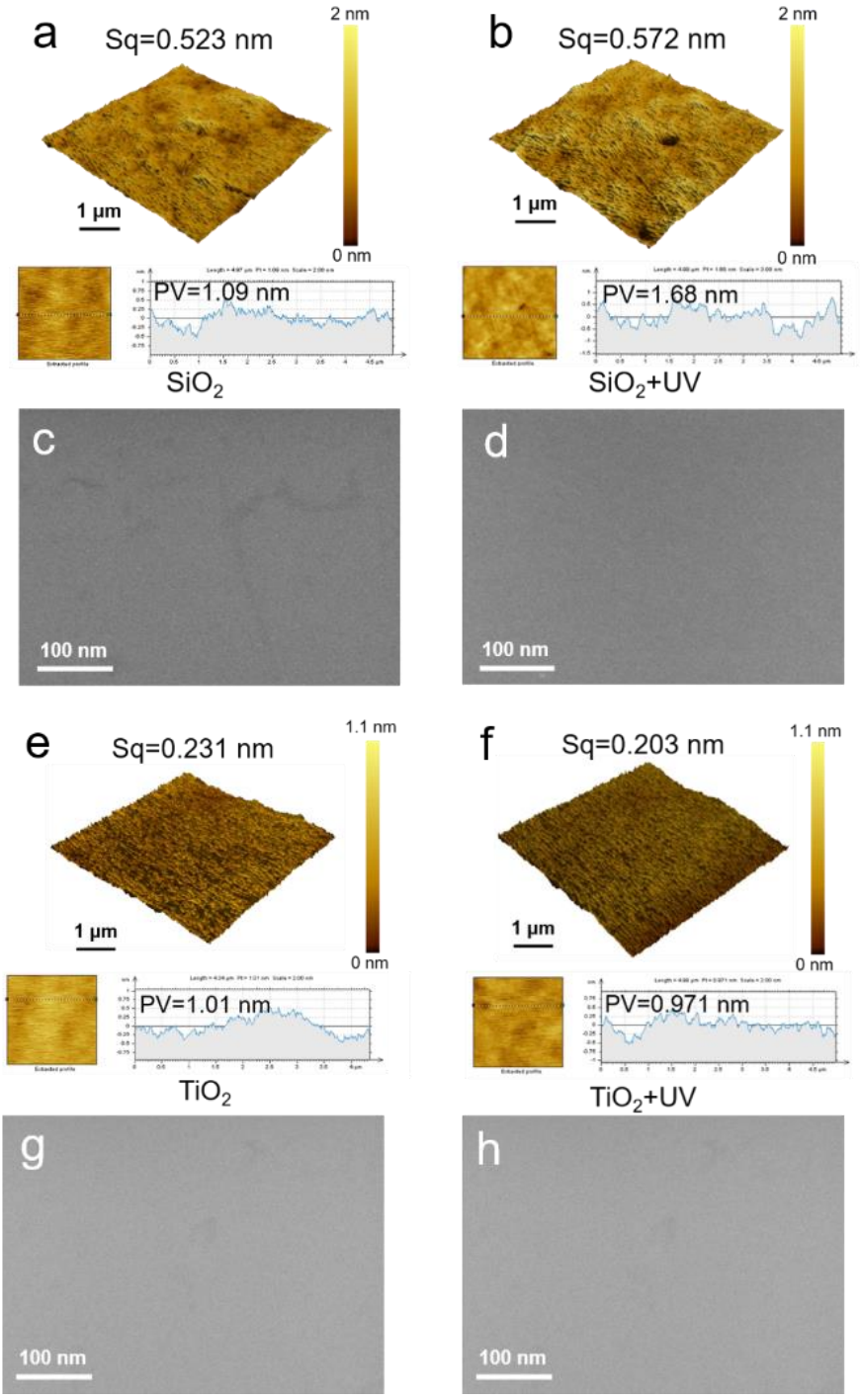


661 **Supplementary Fig. S49.** SEM images, 3D AFM images, and height profiles of Si
662 wafer surfaces polished under different conditions: **a**, **c** 2.5 wt% $SiO_2$; **b**, **d** 2.5 wt%
663 $SiO_2$; **e**, **g** 2.5 wt% $TiO_2$; **f**, **h** 2.5 wt% $TiO_2$ with UV light irradiation.

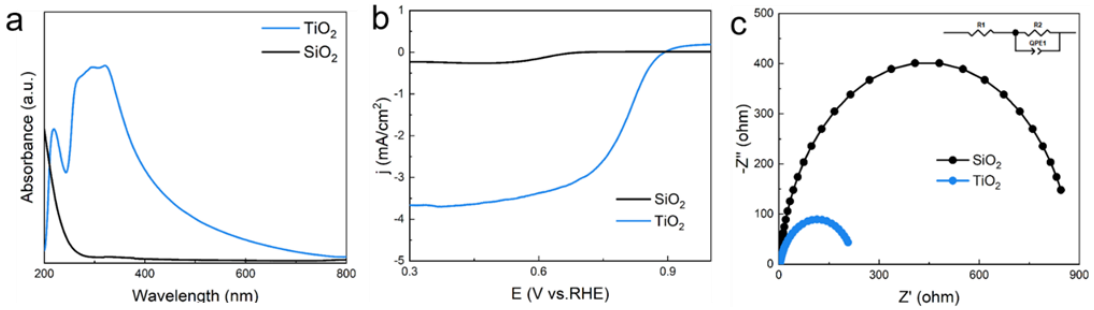


664 **Supplementary Fig. S50. a** UV-Vis spectra. **b** Polarization curves. **c** Nyquist plot of

665 $SiO_2$ and $TiO_2$.

# Supplementary Tables

**Supplementary Table S1.** Percentage of different substances obtained by Ce 3d and O 1s spectroscopy.

| Sample | $Ce^{3+}$ (%) | $Ce^{4+}$ (%) | $O_V$ (%) |
|---|---|---|---|
| $CeO_2$ particles | 21.34 | 78.66 | 30.17 |
| $CeO_2$ slurry | 26.52 | 73.48 | 34.02 |

**Supplementary Table S2.** EXAFS fitting parameters at the Ce $L_3$-edge for various samples.

| **Sample** | **Shell** | ***CN*[a]** | ***R*(Å)[b]** | **σ(Å2)[c]** | **Δ*E*$_0$(eV)[d]** | ***R* factor** |
|---|---|---|---|---|---|---|
| $CeO_2$ reference | Ce-O | 8 | 2.31 | 0.015 | 5.26 | 0.015 |
| $CeO_2$ particles | Ce-O | 4.97 | 2.32 | 0.0091 | 6.32 | 0.019 |
| $CeO_2$ slurry | Ce-O | 4.40 | 2.34 | 0.0103 | 6.82 | 0.014 |

[a]*CN*, coordination number; [b]*R*(Å), the distance to the neighboring atom; [c]σ(Å2), Debye-Waller factor to account for both thermal and structural disorders; [d]Δ$E_0$ inner potential correction; *R* factor indicates the goodness of the fit.

676 **Supplementary Table S3.** $E_{corr}$ and $I_{corr}$ of silicon in different compositions of slurry.

| **Component** | **$E_{corr}$ vs. SCE (V)** | **$I_{corr}$ ($A/cm^2$)** |
|---|---|---|
| Blank | -0.222 | $6.561 \times 10^{-7}$ |
| $CeO_2$ particles | -0.257 | $1.143 \times 10^{-6}$ |
| $CeO_2$ slurry | -0.278 | $2.237\times 10^{-6}$ |
| $CeO_2$ slurry+UV | -0.323 | $4.502 \times 10^{-6}$ |

677

**Supplementary Table S4.** Impedance parameters of silicon in slurries with different compositions obtained by EEC fitting.

| Component | Rs ($\Omega \cdot cm^2$) | R1 ($\Omega \cdot cm^2$) | R2 ($\Omega \cdot cm^2$) | QPE1 ($nF/cm^2$) | QPE2 ($nF/cm^2$) |
|---|---|---|---|---|---|
| Blank | 102.32 | 2398 | 20080 | $8.793 \times 10^{-10}$ | 0.981 |
| $CeO_2$ particles | 29.21 | 1231 | 19316 | $1.241\times 10^{-9}$ | 0.974 |
| $CeO_2$ slurry | 6.99 | 394 | 16307 | $2.261\times 10^{-9}$ | 0.951 |
| $CeO_2$ slurry+UV | 6.61 | 215 | 8253 | $2.923\times10^{-8}$ | 0.927 |

**Supplementary Table S5.** EDS of silicon in different compositions of slurry.

| Component | wt% | | Atomic percentage | |
|---|---|---|---|---|
| | **Si** | **O** | **Si** | **O** |
| Blank | 98.37 | 1.63 | 96.69 | 3.31 |
| $CeO_2$ particles | 97.65 | 2.35 | 95.88 | 4.12 |
| $CeO_2$ slurry | 94.22 | 5.78 | 90.35 | 9.65 |
| $CeO_2$ slurry+UV | 91.01 | 8.99 | 85.31 | 14.69 |

**Supplementary Table S6.** Energy-related parameters are calculated through molecular dynamics simulation.

| | **△H/eV (Total)** | **△H/eV (Per group)** | **T·△S/eV (Per group)** | **△G/eV (Per group)** |
|---|---|---|---|---|
| $H_2O_2$ | -75.34 | -4.70 | -0.53 | -4.17 |
| ·OH | -26.76 | -1.67 | -0.72 | -0.94 |
| $·O_2^-$ | -161.69 | -10.10 | -0.62 | -9.48 |

**Supplementary Table S7.** Performance comparison under different polishing conditions for Si wafers.

| Slurry component | Polishing conditions | MRR (nm/min) | Surface roughness (nm) | Ret. |
|---|---|---|---|---|
| $CeO_2/Na_4P_2O_7/H_2O_2$ | 90 rpm,70 rpm,30 Kpa, 15 mL/min,pH=10 | 127 | 0.067 | [16] |
| $SiO_2/H_2O_2$ | 40 rpm,40 rpm,7 psi, 7 L/min,alkaline | 945 | 0.94 | [17] |
| $SiO_2/KNO_3/H_2O_2$ | 87 rpm,80 rpm,2.8 psi, 80 mL/min,pH=10.5 | 177.87 | 0.887 | [18] |
| $SiO_2/NH^{4+}/H_2O_2$ | 87 rpm,80 rpm,2.5 psi, 80 mL/min,pH=10.5 | 168.7 | 0.744 | [19] |
| amino-modified $SiO_2$ | 80 rpm,80 rpm,2.64 psi, 90 g/min,pH=10.6 | 132.53 | 0.219 | [20] |
| $SiO_2$/EDA/$H_2O_2$ | 71 rpm,69 rpm,5.7 psi, 100 mL/min,pH=10.9 | 552.8 | 0.353 | [21] |
| $SiO_2/C_6H_5O_7(NH_4)_3/H_2O_2$ | 87 rpm,80 rpm,2.8 psi, 80 mL/min,pH=10.5 | 197.98 | 0.563 | [22] |
| $CeO_2$@ZIF-8/PVP | 87 rpm,80 rpm,80 N, 100 mL/min | 151.07 | 0.231 | [23] |
| $SiO_2/H_2O_2$ | 180 rpm,16.7 KPa,10 mL/min,pH=9 | 60 | 0.4 | [24] |
| $CeO_2$/PhPs | 180 rpm,16.7 KPa,10 mL/min,pH=9, UV irradiation(365 nm) | 23 | 0.19 | [24] |
| $SiO_2$/MEA/$H_2O_2$ | 40 rpm,40 rpm,2 psi,155 mL/min,pH=10.5 | 24 | 0.178 | [25] |

| | | | | |
|---|---|---|---|---|
| $CeO_2$@GO/PVP | 87 rpm,80 rpm,80 N,100 mL/min,pH=7-8 | 190.58 | 0.278 | [26] |
| Nd-doped $CeO_2$ /PVP | 120 rpm,90 rpm,10 N, 100 mL/min,pH=6-6.5 | 138.05 | 0.468 | [27] |
| $SiO_2$/$H_2O_2$ | 30 rpm,30 rpm,4 psi,210 mL/min,pH=11 | 265 | 0.175 | [28] |
| $SiO_2$/TMAH/CPAM/ AEO-9/PVP | 60 rpm,60 rpm,1.5 psi, 300 mL/min | 13 | 0.447 | [29] |
| $SiO_2$/MEA/$H_2O_2$ | 93 rpm,87 rpm,2 psi,250 mL/min,pH=11.5 | 680 | 0.299 | [30] |
| $SiO_2$/MEA/$H_2O_2$ | 93 rpm,87 rpm,2 psi,250 mL/min,pH=11.5, | 650 | 0.225 | [30] |
| $CeO_2$/$H_2O_2$/PVP | 93 rpm,87 rpm,4.75 psi, 30 mL/min,pH=10, UV irradiation(365 nm) | 585.8 | 0.0437 | This work |

688

**Supplementary Table S8.** The average friction force and temperature of Si wafers polished with $SiO_2$, $CeO_2$, $TiO_2$ and $CeO_2$ slurry.

| Abrasive | Friction force (Kgf) | Temperature (℃) |
|---|---|---|
| $SiO_2$ | 23.33 | 32.62 |
| $CeO_2$ particles | 21.65 | 33.08 |
| $TiO_2$ | 20.08 | 33.49 |
| $CeO_2$ slurry | 21.63 | 32.97 |

**Supplementary Table S9.** Impedance parameters of different abrasives obtained by EEC fitting.

| Abrasive | R1 ($\Omega \cdot cm^2$) | R2 ($\Omega \cdot cm^2$) | QPE1 ($nF/cm^2$) |
|---|---|---|---|
| $SiO_2$ | 3.47 | 869.7 | $4.0502 \times 10^{-5}$ |
| $CeO_2$ particles | 3.76 | 398.2 | $3.0421\times 10^{-5}$ |
| $TiO_2$ | 4.65 | 220.6 | $2.2264\times 10^{-5}$ |
| $CeO_2$ slurry | 21.76 | 121.3 | $1.5176\times 10^{-5}$ |

# Reference


1. Wang, C. et al. Selective oxidation of methane to $C_{2+}$ products over Au-$CeO_2$ by photon-phonon co-driven catalysis. *Nature Communications* **15**, 7535 (2024).

2. Hao, Y. et al. Cu docking-activated Nb incorporation in multivariate CuO-$Nb_2O_5$/$CeO_2$ catalysts for selective reduction of $NO_x$ with $NH_3$. *Applied Catalysis B: Environmental* **340**, 123254 (2024).

3. Li, Y. et al. Arming Ru with Oxygen-Vacancy-Enriched $RuO_2$ Sub-Nanometer Skin Activates Superior Bifunctionality for pH-Universal Overall Water Splitting. *Advanced Materials* **35**, 2206351 (2023).

4. Wang, H. et al. Facilitating the dry reforming of methane with interfacial synergistic catalysis in an Ir@$CeO_{2-x}$ catalyst. *Nature Communications* **15**, 3765 (2024).

5. Dhall, A. & Self, W. Cerium Oxide Nanoparticles: A Brief Review of Their Synthesis Methods and Biomedical Applications. *Antioxidants (Basel)* **7** (2018).

6. Reed, K. et al. Modeling the Kinetic Behavior of Reactive Oxygen Species with Cerium Dioxide Nanoparticles. *Biomolecules* **9** (2019).

7. Li, Y. et al. Boron Doping-Induced Ultrahigh $Ce^{3+}$ Ratio in Amorphous $CeO_2$/GO Catalyst for Low-Concentration $CO_2$ Photoreduction. **64**, e202505668 (2025).

8. Yang, W. et al. Local Electronic Structure Modulation of Interfacial Oxygen Vacancies Promotes the Oxygen Activation Capacity of Pt/$Ce_{1-x}MxO_{2-\delta}$. *ACS Catalysis* **14**, 5936-5948 (2024).

9. Zu, D. et al. Oxygen Vacancies Trigger Rapid Charge Transport Channels at the Engineered Interface of S-Scheme Heterojunction for Boosting Photocatalytic Performance. *Angewandte Chemie International Edition* **63**, 202405756 (2024).

10. Wei, Z. et al. Steering Electron–Hole Migration Pathways Using Oxygen Vacancies in Tungsten Oxides to Enhance Their Photocatalytic Oxygen Evolution Performance. *Angewandte Chemie International Edition* **60**, 8236-8242 (2021).

11. Yadav, S. et al. A Nonheme Iron(III) Superoxide Complex Leads to Sulfur Oxygenation. *Journal of the American Chemical Society* **146**, 7915-7921 (2024).

12. Zhao, W. et al. Nanoscale Grain Boundary-Weakened Ce–O Covalency and Surface Confinement Intrinsically Boosting Ceria Surface Oxygen Reactivity. *Journal of the American Chemical Society* **147**, 13050-13058 (2025).

13. Luo, D. et al. Engineering the structure defects of ceria-zirconia-praseodymia solid solutions for diesel soot catalytic elimination. *Molecular Catalysis* **569**, 114623 (2024).

14. You, Y., He, Z., Zhou, J., Qi, Y. & Luo, C. Enhanced Ruthenium Removal and Superior Surface Quality via Abrasive-Free Chemical Mechanical Polishing Using Synergistic Catalysis with the $H_2O_2$/PDS/FeIII-NTA System. **n/a**, 2410586.

15. Ishikawa, Y., Matsumoto, Y., Nishida, Y., Taniguchi, S. & Watanabe, J. Surface Treatment of Silicon Carbide Using $TiO_2$(IV) Photocatalyst. *Journal of the American Chemical Society* **125**, 6558-6562 (2003).

16. Cui, X. et al. Unprecedented atomic surface of silicon induced by environmentally friendly chemical mechanical polishing. *Nanoscale* **15**, 9304-9314 (2023).

17. Hong, J. et al. Removal rate and surface quality of the GLSI silicon substrate during the CMP process. *Microelectronic Engineering* **168**, 76-81 (2017).

18. Xie, W. et al. Chemical mechanical polishing of silicon wafers using developed uniformly dispersed colloidal silica in slurry. *Journal of Manufacturing Processes* **90**, 196-203 (2023).

19. Xie, W. et al. Effect of cations on the improvement of material removal rate of silicon wafer in chemical mechanical polishing. *Colloids and Surfaces A: Physicochemical and Engineering Aspects* **670**, 131576 (2023).

20. Wang, D. et al. Atomic surface of silicon wafers induced by grafted silica nanoparticles and sodium carbonate. *Applied Surface Science* **664**, 160234 (2024).

21. Bae, J.-Y. et al. Silicon Wafer CMP Slurry Using a Hydrolysis Reaction Accelerator with an Amine Functional Group Remarkably Enhances Polishing Rate. **12**, 3893 (2022).

22. Xie, W. et al. High efficiency chemical mechanical polishing for silicon wafers using a developed slurry. *Surfaces and Interfaces* **38**, 102833 (2023).

23. Chen, C. et al. Improvement of chemical mechanical polishing performance by introducing N–Si bond via external coating of cerium oxide with ZIF-8. *Surfaces and Interfaces* **50**, 104488 (2024).

24. Murata, J. & Kagawa, M. Photo-Assisted Chemical Mechanical Polishing of Si Wafer Using Phosphorescent Particles as a Luminescent Agent. *ECS Journal of Solid State Science and Technology* **8**, P727 (2019).

25. Xing, Y., Wang, W., Liu, W. & Song, Z. Enhancing Slurry Stability and Surface Flatness of Silicon Wafers through Organic Amine-Catalyzed Synthesis Silica Sol. *Nanomaterials* **14**, 1371 (2024).

26. Chen, C. et al. Novel ceria/graphene oxide composite abrasives for chemical mechanical polishing. *Ceramics International* **50**, 26325-26333 (2024).

27. Jiao, J. et al. Preparation, characterization, and application of Nd-doped ceria-coated silica nanoparticles for chemical mechanical polishing. *Journal of Materials Science* **58**, 18014-18028 (2023).

28. Lee, M.-Y., Kang, H.-G., Kanemoto, M., Paik, U. & Park, J.-G. Effect of Alkaline Agent in Colloidal Silica Slurry for Polycrystalline Silicon Chemical Mechanical Polishing. *Japanese Journal of Applied Physics* **46**, 5089 (2007).

29. Zhao, Q. et al. Control of the Micro-Defects on the Surface of Silicon Wafer in Chemical Mechanical Polishing. *ECS Journal of Solid State Science and Technology* **11**, 023009 (2022).

30. Zhang, X. et al. Effect and Mechanism of Dual-Official Group of Ethanolamines on the Chemical Mechanical Polishing of Monocrystalline Silicon. *ECS Journal of Solid State Science and Technology* **11**, 093005 (2022).